2008-07-09

Multi-physics Modeling and Calibration for Self-sensing of Thermomechanical In-plane Microactuators

Kendall B. Teichert
Brigham Young University - Provo

MULTI-PHYSICS MODELING AND CALIBRATION FOR SELF-SENSING OF THERMOMECHANICAL IN-PLANE MICROACTUATORS

by

Kendall B. Teichert

A thesis submitted to the faculty of

Brigham Young University

in partial fulfillment of the requirements for the degree of

Master of Science

Department of Mechanical Engineering

Brigham Young University

August 2008

BRIGHAM YOUNG UNIVERSITY

GRADUATE COMMITTEE APPROVAL

of a thesis submitted by

Kendall B. Teichert

This thesis has been read by each member of the following graduate committee and by majority vote has been found to be satisfactory.

Date	Brian D. Jensen, Chair
Date	Larry L. Howell
Date	Timothy W. McLain

BRIGHAM YOUNG UNIVERSITY

As chair of the candidate's graduate committee, I have read the thesis of Kendall B. Teichert in its final form and have found that (1) its format, citations, and bibliographical style are consistent and acceptable and fulfill university and department style requirements; (2) its illustrative materials including figures, tables, and charts are in place; and (3) the final manuscript is satisfactory to the graduate committee and is ready for submission to the university library.

Date

Brian D. Jensen
Chair, Graduate Committee

Accepted for the Department

Matthew R. Jones
Graduate Coordinator

Accepted for the College

Alan R. Parkinson
Dean, Ira A. Fulton College of
Engineering and Technology

ABSTRACT

MULTI-PHYSICS MODELING AND CALIBRATION FOR

SELF-SENSING OF THERMOMECHANICAL

IN-PLANE MICROACTUATORS

Kendall B. Teichert

Department of Mechanical Engineering

Master of Science

As technology advances and engineering capabilities improve, more research has focused on microscopic possibilities. Microelectromechanical systems (MEMS) is one area that has received much attention recently. Within MEMS much research has focused on sensing and actuation. This thesis presents work on a particular actuator of interest, the thermomechanical in-plane microactuator (TIM). Recent work has shown the possibility of a novel approach of sensing mechanical outputs of the TIM without ancillary sensors. This sensing approach exploits the piezoresistive property of silicon. However, to implement this approach a full model of the TIM would need to be obtained to describe the physics of the TIM, as well as development of a calibration approach to account for variations between devices.

This thesis develops a multi-physics model of the TIM to realize this sensing approach. This model determines the mechanical state of the TIM using the same electrical signal that actuates the TIM. In this way the TIM is able to operate as a self-sensing actuator. To allow this multi-physics model to be tractable, work was done to simplify the

thermal modeling of the TIM. A preliminary calibration approach was developed to adequately compensate for variations between devices. Thermal modeling and calibration were coupled with mechanical modeling and a developed sensing approach to form the full multi-physics model of the TIM. Validation testing of the model was performed with a modified calibration approach which showed good correlation with experimental data.

ACKNOWLEDGMENTS

I have received so much help with this research and throughout my life. I would like to acknowledge Brigham Young University and thank them for the opportunity to study at this school. I would like to acknowledge the funding of National Science Foundation grant No. 0428532, and DARPA through Block MEMS, LLC.

This research would not have been possible without the help of my committee and my fellow students in the Compliant Mechanisms Research lab.

I would also like to thank my friends who have been an amazing support, and especially my family that have encouraged, supported and really enabled me to get to where I am. And most of all, I acknowledge the hand of God in my life that has really made all things possible and continues to bless my life, even when I don't recognize or deserve it.

Table of Contents

List of Tables

List of Figures

Chapter 1

Introduction

1.1 Research overview

Sensing and actuation in microelectromechanical systems (MEMS) is becoming ever more important as technology becomes more advanced. One type of MEMS actuation that has shown promise in force and displacement capabilities is the thermomechanical in-plane microactuator (TIM) [1]. The TIM operates on the principle of ohmic heating. As a current is passed through the thin legs of the TIM ohmic heating causes thermal expansion in the legs. Due to the geometric configuration of the TIM this expansion is propagated in a forward motion by the buckling of the legs as seen in Figure 1.1.

For implementation of actuation in many applications, accurate sensing approaches are required. Several types of displacement sensing have been developed [2], [3]. However, force sensing has been difficult on the MEMS scale. Recent work has shown the possibility of using the TIM as a self-sensing actuator for both force and displacement applications [4]. Self-sensing is the ability for a mechanism to act in its designed function while providing a form of sensing with no ancillary sensors. For this application the sensing medium is the piezoresistive effect of silicon [5]. Recent work has shown the possibility of using this piezoresistive effect for an entire structure as a sensing signal rather than a selectively doped area [3], [6], [7].

This concept can be applied to the TIM by assuming that changes in resistance during actuation can be attributed to two sources: changes due to temperature dependence and changes due to piezoresistive changes proportional to stress. This concept is depicted in Figure 1.2. Figure 1.2 also demonstrates that for a given actuation current, certain loading conditions will correspond to certain piezoresistive changes in resistance. This phenomena

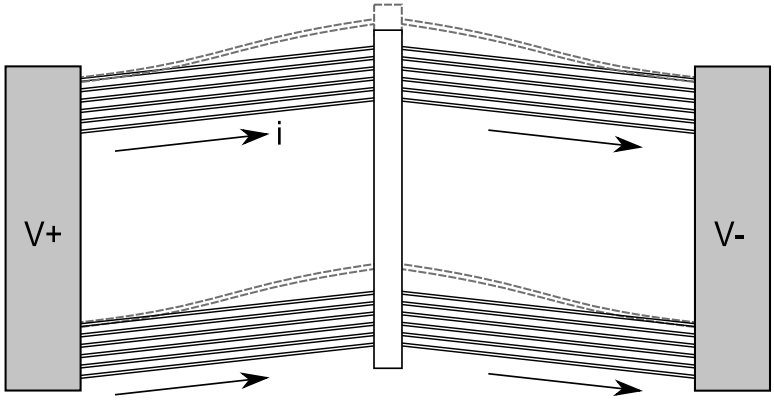

Figure 1.1: Schematic of TIM motion

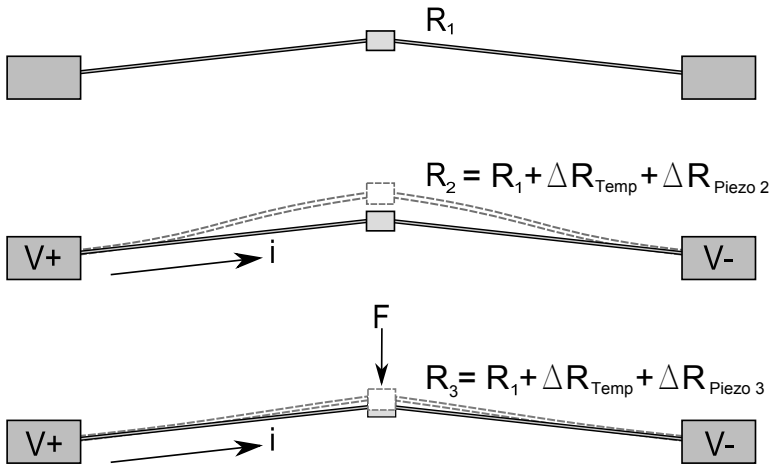

Figure 1.2: Fundamental concept of TIM self-sensing

is the foundational principle of TIM self-sensing. However, in order to properly correlate these changes in resistance with the mechanical outputs of the TIM, proper modeling of the physics of the TIM is needed. Modeling will allow for a decoupling of the temperature change in resistivity and the piezoresistive change. This modeling will include characterization of the electrothermal and mechanical aspects of the TIM. This thesis is to present work done to develop this multi-physics model of the TIM, as well as a calibration approach to properly account for variation from TIM to TIM.

This approach to actuation and sensing has potential for application in micromanipulation, micro positioning, microrobotics, optics, and other MEMS applications. This approach has the advantage of possible reduction in footprint size of the system, increased efficiencies over mechanical sensing techniques, and an elimination of separate signals needed for actuation and sensing by incorporation of these two signals in one.

1.2 Thesis organization

This thesis is a compilation of papers that have been, or will be submitted to various venues. The venue to which each chapter has been submitted at the time of the presentation of this thesis will be noted in the "acknowledgments" section of the chapter. These papers will be presented here as submitted, including abstracts and introductions, with only minor changes. For simplicity, all references will be placed together at the end of this thesis. A comprehensive literature review will be dispensed of in lieu of each chapter containing its own literature review. Due to this particular presentation approach, certain information will seem redundant when this thesis is read in its entirety, but it is hoped that this approach will allow greater clarity and ease of access for those interested in only a particular portion of this research.

1.3 Thesis outline

For realization of this self-sensing approach to actuation, a model of the various physics of the TIM was needed. Proper thermal characterization of the TIM was crucial to this model. Chapter 2 presents a simplification approach to thermal modeling that allows for accurate modeling to be done using a reduced order approach (i.e. 3-dimensional to 1-dimensional). This work is an expansion of the work done in [8], and significantly reduces the computational expense of the thermal modeling. This chapter also presents validation modeling showing correlation between a full 3-dimensional model and the simplified approach presented.

To compensate for variations from TIM to TIM, a calibration approach was needed. Chapter 3 presents a calibration technique, and a novel calibration structure. This cali-

bration approach allowed for corrections in the modeling of the TIM material properties, namely resistivity, and geometries (due to deviations from the design during fabrication). In connection with this calibration approach, validation testing was performed, showing improvement in the model output over the uncalibrated model.

Chapter 4 presents a full model incorporating the thermal model reduction approach developed in chapter 2 and a mechanical model based on a finite element approach. This model was able to determine the forces, displacements, and stress profiles of the TIM for a given actuation current. A new calibration approach is presented that uses the basic principles as those presented in Chapter 3, but performs the calibration on a TIM rather than a separate calibration structure. This calibration approach required an iterative approach to calibrate for resistivity and piezoresistivity. Validation testing was presented for a calibrated, full model showing correlation between the test and model data within the experimental error in nearly all cases.

Chapter 2

Thermal Correction Values for Analysis of Lineshape Microstructure Arrays

2.1 Abstract

Thermal modeling of microelectromechanical systems is a major area of research with many different approaches and complexities. In this paper a simplified, reduced order model, for thermal analysis of lineshape microstructure arrays, such as those used in thermal actuators, is explained. Finite element modeling of these arrays was performed to determine thermal correction (K_t) values for the simplified thermal model. An equation is developed to describe a general MEMS design space of the independent parameters for implementation of the simplified model. Error in the equation fit is quantified and the fit is validated. Application of the model is also shown for single microstructures. Implementation of the simplified model using a finite difference model is presented and validated, with errors in predicted temperature rise of less than 5.4%.

2.2 Introduction

Various microelectromechanical systems (MEMS) depend on thermal phenomena for their operation. Much research has been done to capture these phenomena [9]–[13]. One such device is the chevron-shaped thermal actuator or thermomechanical in-plane microactuator (TIM) [1], [14]–[17], as shown in Figure 2.1. Understanding the thermal behavior of devices like these is crucial to proper modeling. In modeling these thermal attributes, the trade-off between simplicity and accuracy has resulted in several different approaches [1], [14], [18]. Work done by Lin and Chiao [8] developed a shape-correction

factor that correlates the heat flux through the bottom of a lineshape microstructure to that of the heat flux out of the entire structure. This work has been used in several studies [14], [19], [20]. In Lin's work a 2-dimensional finite element model (FEM) of the cross-section of the structure was developed to determine this correction value for a single microstructure. This work expands this concept for application to multiple microstructures in air that are in an array configuration. This further development is necessary to account for heat interactions between structures in the TIM.

One particular motivation for this type of simplification of thermal modeling of lineshape microstructure arrays is shown in recent research by Harb et al. [21], in which they showed that increased efficiencies can be obtained in thermal actuators by lumping the actuation legs together so as to reduce heat loss to the surroundings. As mentioned by Harb et al. power reduction is significant for TIMs in order to make them viable for on-chip applications. Some previous modeling of the TIM with spread leg systems [14] used correction values based on Lin and Chiao's [8] one microstructure values. However, as these legs are brought closer to eliminate heat transfer to the surroundings, changes in these correction values occur. To properly analyze these actuators in this new "lumped" configuration, full three-dimensional modeling could be used as by Messenger [18], which requires immense computational power, or proper correction values could be developed to incorporate the interdependence between microstructures.

This paper presents an explanation of the significance of this expanded work will be presented. Finite element modeling was performed to analyze the static heat transfer of these device arrays. This model was used to explore the implications of this research over the desired design space. From this initial research a final modeling approach was developed. Implementation of the simplification developed in this work will be demonstrated in a finite difference analysis of a TIM.

2.3 Modeling approach

2.3.1 Thermal correction value definition

The basic equation for heat transfer in a thin microstructure with temperature-dependent material properties is

$$\frac{\partial}{\partial x}\left(\kappa\frac{\partial T}{\partial x}\right) = -q_{gen} + q_{loss} \tag{2.1}$$

where x is the location along the beam, κ is the thermal conductivity, T is the temperature, q_{gen} is the heat generation in the structure, and q_{loss} is the heat loss from the structure. However, the value of q_{loss} can be computationally expensive to determine in three-dimensional space. The purpose of the thermal correction value, K_t, is to allow accurate modeling to be done using a reduced order model. This approach is based on the work for a single microstructure presented in [8], which is based on the assumption that the majority of heat loss is directly from the bottom of the microstructure to the substrate. Using this assumption, the heat loss would be calculated as

$$q_{loss\_reduced} = \left(\frac{A}{R_{th}}\right)(T_{sub} - T) \tag{2.2}$$

$$R_{th} = \frac{t_{air}}{\kappa_{air}} + \frac{t_{sub}}{\kappa_{sub}} \tag{2.3}$$

where $q_{loss\_reduced}$ is heat loss from the microstructure to the substrate in the reduced order model, A is the surface area of the bottom of the microstructure, t_{air} and t_{sub} are the thickness of the air gap and substrate respectively, and κ_{air} and κ_{sub} are the thermal conductivities of the air and substrate respectively. As mentioned, these equations assume only heat loss from the bottom of the structure to the substrate. Therefore, to compensate for the remainder of the heat flow a correction value, K_t, was defined as the actual heat transfer (q_{loss_actual}) that would occur out of the entire microstructure divided by the estimated value ($q_{loss\_reduced}$) that would be calculated by Equation (2.2), or

$$K_t = \frac{q_{loss\_actual}}{q_{loss\_reduced}}. \tag{2.4}$$

In this way the K_t value can be used to compensate for the loss of information due the reduction in order of a 1D model. As a result, Equation (2.2) becomes

$$q_{loss\_actual} = (K_t)\left(\frac{A}{R_{th}}\right)(T_{sub} - T)\,. \tag{2.5}$$

This approach is easily implemented into a basic finite difference model. The basic finite difference equation would then become

$$\kappa_i\left(\frac{T_{i+1} - 2T_i + T_{i-1}}{(\Delta x)^2}\right) + \left(\frac{\kappa_{i+1} - \kappa_{i-1}}{2\Delta x}\right)\left(\frac{T_{i+1} - T_{i-1}}{2\Delta x}\right) = -I^2\frac{R_e}{\Delta V} + K_t\left(\frac{T_i - T_s}{R_t \Delta x}\right) \tag{2.6}$$

with K_t as described previously; T the temperature of the node; T_s the substrate temperature; Δx the length of the beam associated with the node; R_t as described previously; I the electrical current through the node; R_e the electrical resistance associated with the node; ΔV the volume associated with the node; κ the thermal conductivity; and the subscripts $i-1$, i, and $i+1$ being the previous, current, and next nodes respectively. The boundary conditions for Equation 2.6 include a proscribed temperature at one end, and a symmetric or insulated boundary (corresponding to $\partial T/\partial x = 0$) on the other end. Further explanation of boundary conditions will be given in the K_t value implementation section. To implement this model, the dependence of K_t on the structure geometry must be know.

2.3.2 Finite element model

To characterize these K_t values, or more specifically the q_{loss_actual} values, a FEM was developed using a commercial finite element package (ANSYS). The model was based on a 2D cross-section of the structure. Figure 2.1 shows the basic geometries of the model. A representative meshing of the FEM is shown in Figure 2.2. This model consisted of three main components: air, substrate, and structure. The air was modeled with temperature-dependent material properties using infinite boundary condition elements on the outer edges (infin9 in ANSYS). The substrate was modeled as monocrystalline silicon,

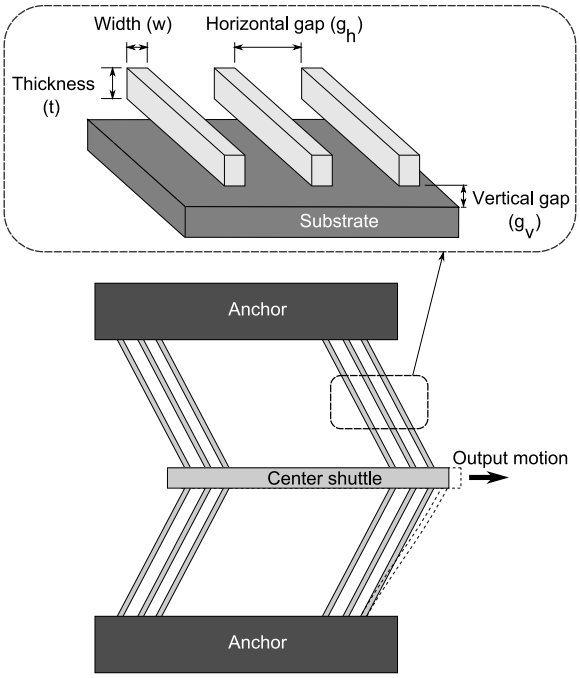

Figure 2.1: Thermomechanical in-plane microactuator as an array of lineshape microstructures

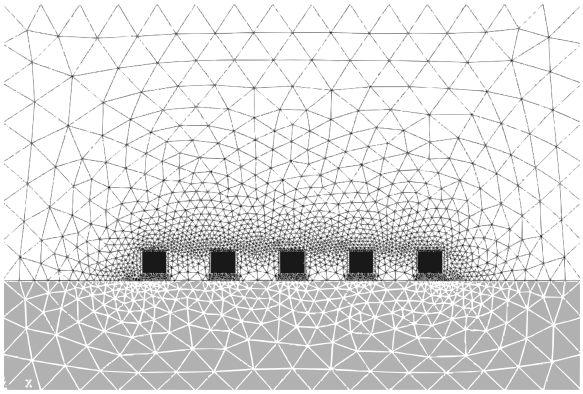

Figure 2.2: Example meshing of 2D FEM

with infinite boundary condition elements on its sides only. The structures were modeled as polycrystalline silicon with temperature-dependent material properties. The material properties used throughout this work are the same as in Messenger [18], which included the temperature-dependent properties of the thermal conductivity of air and polycrystalline silicon, the resistivity of polycrystalline silicon, and the density of air. All outer edges of the

model (air top and sides, and substrate sides and bottom) were constrained to the ambient temperature.

The initial modeling was done to explore effects due to changes in geometries, temperature, and number of structures in the array. The model was parameterized to be able to change microstructure thickness (t), width (w), vertical gap from top of the substrate to the bottom of the structure (g_v), horizontal gap spacing between structures (g_h), number of structures in the array, and the structure temperature. The bottom of the substrate was held at a constant temperature of 300 K, and the cross section of the microstructures was held at a uniform temperature. While some variation in the temperatures from one microstructure in the array to another is expected, the temperature was approximated to be constant on all cross sections in order to make the analysis tractable. The validity of this approximation will be demonstrated later in the implementation section. To eliminate unnecessary elements in the center of the cross-sections, only a small shell of the perimeter of the microstructures was meshed. This was possible because of the uniform temperature applied to the structure.

To determine the adequacy of the meshing approach used, a mesh refinement study was performed. This was done by refining the mesh around the microstructures and observing the changes in the output of the FEA. If only minor changes occurred, the original mesh was consided adequate. Sixteen of the designs were chosen to represent the area of the design space with the coarsest meshing. The parameter values for these designs are given in Table 2.1. In this mesh refinement study all array designs contained five lineshape microstructures. Material properties were the same as previously mentioned.

For each design a mesh refinement around the microstructures was performed. The ratio of nodes after and before the refinement for each design was between eight and twelve, or in other words there were eight to twelve times the number of nodes in the refined case as the unrefined case. Even with this significant refinement in meshing, the change in K_t values changed by no more than 2% for any of the structures in the 16 array designs chosen. Results for each design are shown in Table 2.2. The K_t change reported in Table 2.2 represents the largest change for any of the five lineshape microstructures in the array. From this data it can be seen that significant changes in mesh density only contribute

Table 2.1: Parameter values for mesh refinement (all values in μm)

Design	Thickness (t)	Width (w)	Vertical gap (g_v)	Horizontal gap (g_h)
1	2	3	1	0.1
2	2	3	1	1
3	2	3	7.5	0.1
4	2	3	7.5	1
5	2	5	1	0.1
6	2	5	1	1
7	2	5	7.5	0.1
8	2	5	7.5	1
9	4.5	3	1	0.1
10	4.5	3	1	1
11	4.5	3	7.5	0.1
12	4.5	3	7.5	1
13	4.5	5	1	0.1
14	4.5	5	1	1
15	4.5	5	7.5	0.1
16	4.5	5	7.5	1

minor changes to the resultant outcomes; therefore the original meshing of the model was considered adequate. It is assumed that the rest of the design space would produce similar results.

With the model set up for initial runs, various values were chosen for the parameters mentioned. In this initial stage, t and w were not changed separately but rather the t/w ratio was used, consistent with Lin and Chiao [8]. Each run was done for 1 to 10 structure arrays, with temperatures ranging from 300 K to 800 K.

2.3.3 Initial results

This initial study provided several important pieces of information for the development of the final setup. First, when calculating q_{fd} to determine K_t (see Equations (2.2) and (2.4)) if the temperature-dependent thermal conductivity of air were calculated based on the average temperature between the structure and the substrate, K_t showed little dependence on temperature (see Figure 2.3). However, if either the substrate or structure temperatures were used there was a significant dependence on temperature. Due to this

Table 2.2: Mesh refinement results by design number

Design number	(Nodes refined)/ (Nodes unrefined)	Max change K_t
1	10.91	1.16 %
2	11.00	0.21 %
3	10.71	1.32 %
4	10.53	0.37 %
5	8.37	1.11 %
6	9.51	0.33 %
7	9.32	1.25 %
8	10.19	0.51 %
9	11.77	1.37 %
10	11.72	0.32 %
11	11.37	1.42 %
12	11.02	0.43 %
13	9.16	1.30 %
14	10.15	0.62 %
15	9.85	1.65 %
16	10.66	0.94 %

finding the average temperature between the substrate and the structure was used for all subsequent calculations for the thermal conductivity of air.

Second, this initial model verified that the K_t values differed depending on positioning in the array as shown in Figure 2.3. The positioning nomenclature used is described in Figure 2.4. There are significantly different K_t values for structures positioned on the outside of an array (structures 1 and 10 for a 10 structure array, see Figure 2.4) as opposed to those located in the second (structures 2 and 9 for a 10 structure array, see Figure 2.4), or inside positions. This follows intuition in that structures on the outside are only shielded on one side, and thus lose more heat to the surroundings. It was also shown that the second structures in the array have a slightly different value from the remaining inside structures.

Third, there was little variation of the K_t values for the inside structures of the arrays, regardless of the size of the array (as long as there were inside structures, i.e. 5 or more structures).

Finally, the non-dimensional parameter t/w, or height-to-width ratio, was not adequate for describing the design space under these conditions. If the thickness was held

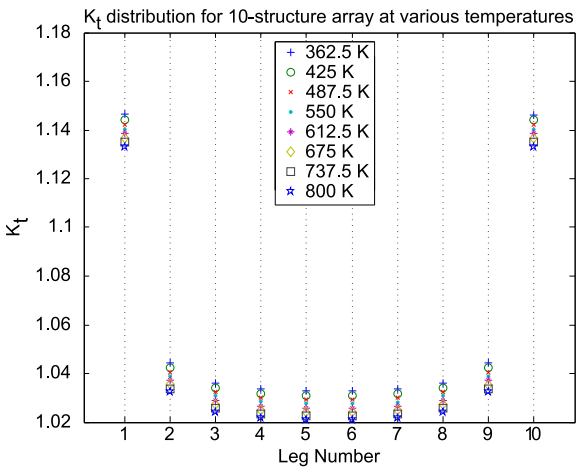

Figure 2.3: Example distribution of K_t values for a 10-structure array at various temperatures

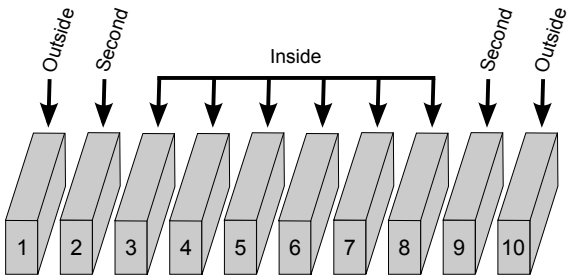

Figure 2.4: Nomenclature for microstructure array positions

constant and width of structure was varied, the output was linear with t/w, but if both were varied there was no longer a linear relationship.

2.3.4 Final FEM

Using these observations from the the initial run, a final approach was developed. To properly describe the design space all parameters were varied independently. Ten values were chosen for each of the four parameters. The values chosen are listed in Table 2.3 with all dimensions in micrometers. These values were chosen to encompass both the MUMPs [22] and SUMMiT V ™ [23] fabrication processes. Four parameters at ten levels produced 10,000 designs within the design space. To reduce unnecessary computation, an array of five structures was selected. This array size would enable data to be gathered for

Table 2.3: Parameter names and values of final FEM

	Values (μm)									
t	0.5	0.75	1.0	1.25	1.5	2.0	3.0	3.5	4.0	4.5
w	1.0	1.25	1.5	2.0	2.5	3.0	3.5	4.0	4.5	5.0
g_h	1.0	1.5	2.5	5.0	7.5	10	15	20	25	30
g_v	0.1	0.15	0.25	0.5	1.0	1.5	2.0	3.0	5.0	8.0

Table 2.4: Parameter names and values of final FEM

Parameter	Value
Substrate thickness	20 μm
Air thickness	50 μm
Substrate temp.	300 K
Structure temp.	800 K

outside, second, and inside structures without redundant information from duplicate inside structures. Other important parameters of the model are listed in Table 2.4.

2.4 Results

2.4.1 Physical interpretation of data trends

Graphical representation of the data is not feasible for the four dimensional design space, but two representative plots of K_t vs. g_v and g_h with t and w held constant and K_t vs. t and w with g_v and g_h held constant are given in Figures 2.5 and 2.6 respectively. Certain trends are readily apparent in these figures. These trends include the following: as the thickness, horizontal and vertical gaps increase the K_t value increases; and as the width increases the K_t value decreases. These trends follow intuition in that as the spacing increases there will be less heat transfer between structures, requiring a higher K_t value. As the thickness increases more heat will be lost from the side of the structure, requiring a higher K_t value as well. Finally, as the width is increased, more heat will be transfered from the bottom of the structure, thus requiring less correction, or a lower K_t. It is also important to note that the results are smooth with respect to the four variables, suggesting that it is feasible to fit a model to the data.

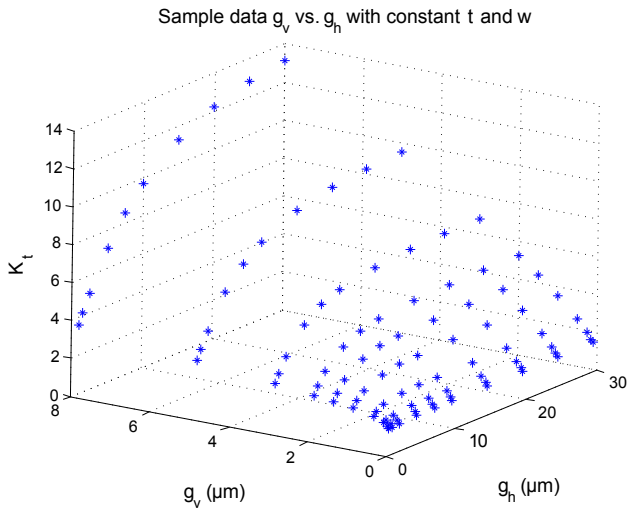

Figure 2.5: Sample Data g_h vs. g_v with t and w held constant

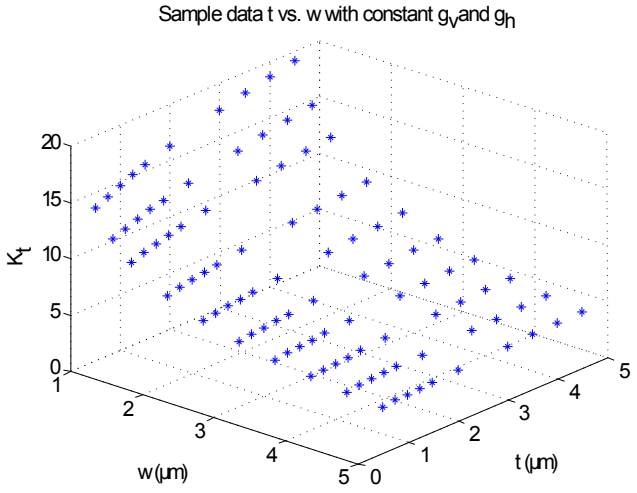

Figure 2.6: Sample Data g_h vs. g_v with t and w held constant

2.4.2 Fitting approach and results

It was determined that one simple equation is insufficient to describe the behavior. The main difficulty in fitting the data occurred in the variation of K_t values due to changes in width. It was therefore decided to split the data into two separate sets. Set 1 included all data that was obtained from structures with widths less than or equal to 2.5 μm, and Set 2 included all data with widths greater than or equal to 2.5 μm. By allowing the data at 2.5 μm to be in both sets it was ensured that the fit would span the entire space.

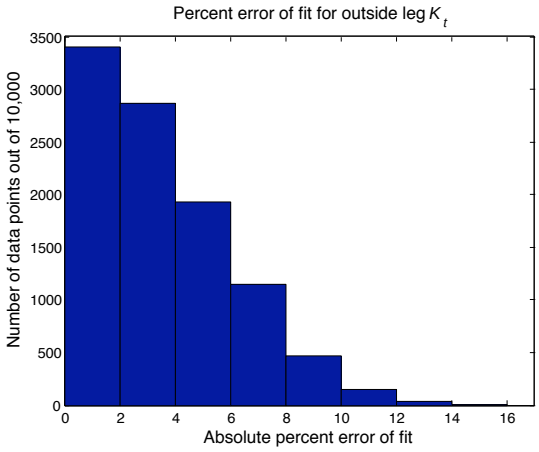

Figure 2.7: Histogram of percent error of fit for outside structures

Once the data was split into its respective sets it was fit with the rational equation

$$K_t = \frac{(A+B)}{(C+D+E)} \tag{2.7}$$

where

$$A = c_1 t g_h + c_2 t g_v + c_3 w g_h + c_4 w g_v + c_5 g_h g_v \tag{2.8}$$

$$B = c_6 t + c_7 w + c_8 g_h + c_9 g_v + c_{10} \tag{2.9}$$

$$C = c_{11} t w + c_{12} t g_h + c_{13} t g_v \tag{2.10}$$

$$D = c_{14} w g_h + c_{15} w g_v + c_{16} g_h g_v \tag{2.11}$$

$$E = c_{17} t + c_{18} w + c_{19} g_h + c_{20} g_v + 1. \tag{2.12}$$

Using this approach it is possible to define a set of coefficients for each scenario rather than create a separate equation. Coefficients were obtained for both sets of widths for outside, second, and inside structures. These coefficients are presented in Tables 2.5 and 2.6.

For this application, a fit with maximum error of less than 20% was adequate. The percent error at each point of the fit was calculated, to verify that this standard was meet. Histograms of these errors are displayed in Figures 2.7, 2.8, and 2.9 for outside, second, and inside structures respectively. Over 80% of the data is fit with less than 6% error, and the entire surface is within 18% error, in all three cases.

Table 2.5: Coefficient values for surface fit for width$\leq$ 2.5 μm

Coefficient	Outside	Second	Inside
c_1	-0.268	-0.441	-0.589
c_2	3.917	-0.203	0.081
c_3	1.804	2.802	3.357
c_4	2.350	2.339	3.577
c_5	4.798	8.556	10.387
c_6	2.700	0.236	-0.017
c_7	5.824	4.408	4.397
c_8	1.019	2.050	2.246
c_9	6.559	6.012	6.093
c_{10}	0.996	0.629	0.727
c_{11}	0.638	-0.303	-0.221
c_{12}	-0.227	-0.373	-0.484
c_{13}	0.055	-0.012	0.180
c_{14}	1.719	2.793	3.378
c_{15}	1.747	4.148	5.153
c_{16}	0.081	0.093	0.167
c_{17}	0.977	0.844	0.495
c_{18}	4.760	3.869	3.805
c_{19}	0.321	0.729	0.816
c_{20}	-0.619	-0.237	-0.055

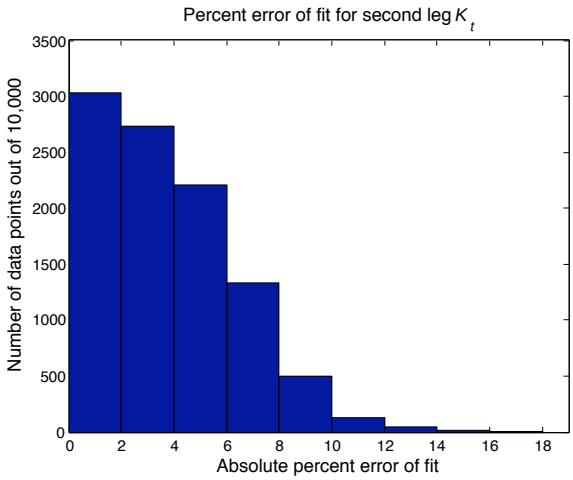

Figure 2.8: Histogram of percent error of fit for second structures

Table 2.6: Coefficient values for surface fit for width$\geq$ 2.5 μm

Coefficient	Outside	Second	Inside
c_1	-0.585	-0.852	-1.062
c_2	3.077	0.523	0.201
c_3	1.517	2.524	3.172
c_4	2.533	2.089	5.362
c_5	4.803	8.429	11.379
c_6	4.083	2.698	1.325
c_7	5.941	5.282	3.544
c_8	1.566	2.045	3.342
c_9	6.118	5.442	6.137
c_{10}	1.132	0.929	0.900
c_{11}	0.322	-0.005	0.006
c_{12}	-0.496	-0.847	-1.032
c_{13}	0.107	0.187	0.173
c_{14}	1.505	2.521	3.213
c_{15}	1.532	2.988	5.515
c_{16}	0.208	0.330	0.356
c_{17}	2.170	2.716	1.342
c_{18}	6.190	5.252	3.948
c_{19}	0.699	1.225	2.132
c_{20}	-1.358	-0.152	0.645

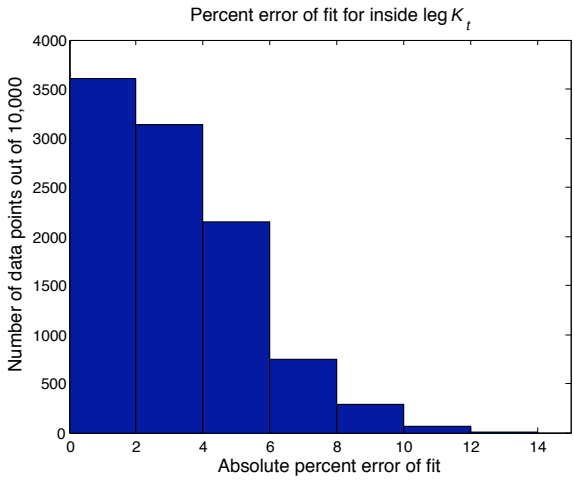

Figure 2.9: Histogram of percent error of fit for inside structures

Table 2.7: Parameter names and values for fit validation

	Values (μm)			
t	0.51	1.1	2.1	4.4
w	1.1	1.75	3.25	4.9
g_h	1.1	2.75	12	29
g_v	0.11	0.75	2.5	7.9

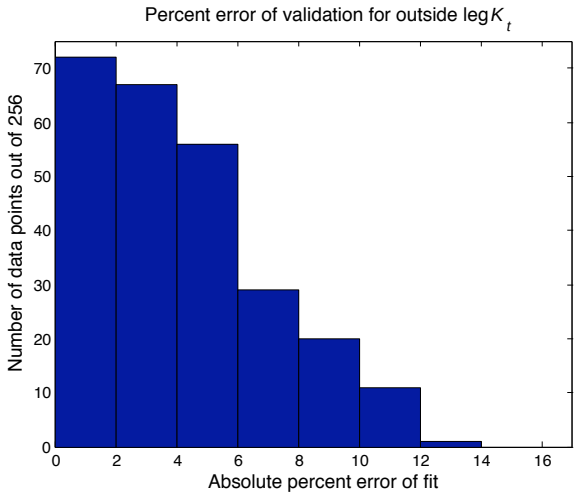

Figure 2.10: Histogram of percent error for validation for outside structures

2.4.3 Fit Validation

To validate this fit, a sampling of points was chosen from the design space that used values that were not used in the original set, but were within the range of the original set. Four test values were chosen for each of the four parameters (given in Table 2.7), resulting in 256 validation points. Percent errors were calculated for this data compared to the original fit. Histograms of these errors are displayed in Figures 2.10, 2.11, and 2.12 for outside, second, and inside structures respectively. Over 74% of the data fit has less than 6% error and all data is within 14% error for all three cases, which is well within the 20% criteria.

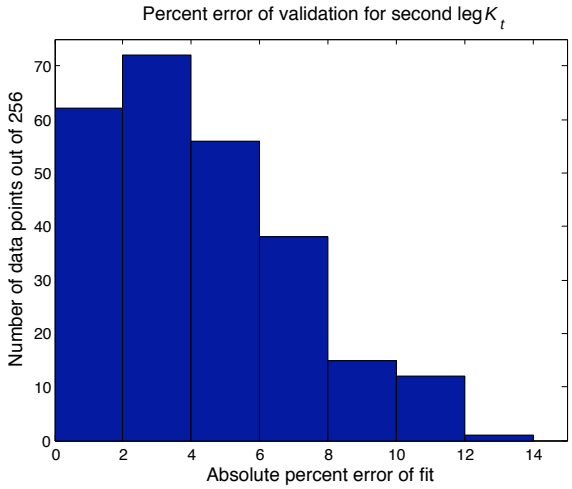

Figure 2.11: Histogram of percent error for validation for second structures

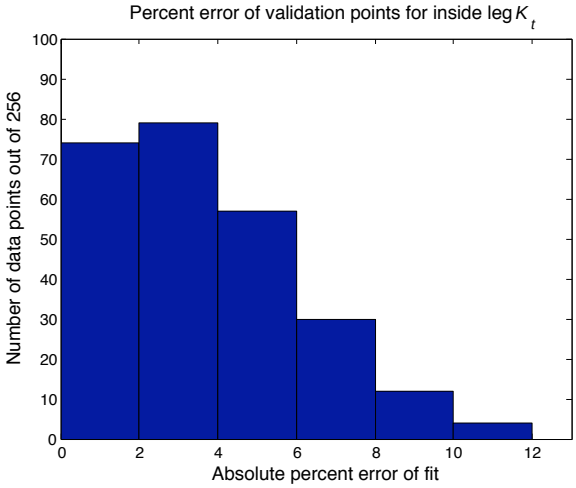

Figure 2.12: Histogram of percent error for validation for inside structures

2.4.4 One structure array

For breadth of application it was desirous to determine an approach for applying the equations presented here to single microstructures. This would eliminate the need for having separate equations based on whether there was only one structure to be analyzed or if there were many. Since the main concern with using a single structure approach on an array configuration is the heat effects between structures, it was assumed that an array approach could be used on a single structure if a large number was used for the g_h value,

Table 2.8: Parameter names and values for 'one structure' run

	Values (μm)					
t	0.5	1.0	1.5	2.0	3.0	4.5
w	1.0	1.5	2.0	3.0	4.0	5.0
g_v	0.1	0.25	0.5	1.5	3.0	8.0

thus removing any effect the array approach would introduce from other structures. In order to determine which set of equations and what values would be best to use, a FEM was run for one structure with various parameter settings as shown in Table 2.8. The results showed mean and maximum errors of less than 5.6% and 13.4%, repsectively, if a single microstructure is approximated using the outside coefficients with a g_h value of 20 μm.

2.5 K_t value implementation

To demonstrate the usability of the K_t values generated in this work, a finite difference model (FDM) based on Equation 2.6 was developed. This FDM was used to analyze a thermomechanical in-plane microactuator (TIM), similar to the one shown in Figure 2.1. The K_t value was implemented similarly to the shape correction value used in [14], with certain adaptations used in this work to account for heat effects in the center shuttle. Three major aspects of the FDM are important to note. First, due to the temperature-dependent material properties, an iterative approach was implemented where the temperature from the previous step was used to determine the properties for the current iteration. This was continued until the solution converged. Second, unlike the FEM, the FDM did not explicitly model the anchor pads of the TIM, but approximated the temperature rise in the anchor pad by using the input temperature next to the first node as the ambient temperature. Third, nodes associated with the center shuttle of the TIM accounted for heat flow down the shuttle as well as out of the bottom. Also, the nodes in the shuttle used a K_t value of one, with the exception of the outside node (at the end of the shuttle) which used a K_t value for a g_h of zero.

The FDM results were compared to a fully 3D Finite Element Model (FEM) in ANSYS. The model used was a modified version of that used by Messenger [18], removing

Table 2.9: Parameter and K_t values for FDM/FEM comparison

	Case 1	Case 2	Case 3
t (μm)	2.5	3.5	2.0
w (μm)	5.0	3.0	2.0
g_h (μm)	5.0	5.0	2.5
g_v (μm)	2.0	2.0	2.5
Leg length (μm)	200	250	200
Number of legs	5	6	6
Shuttle width (μm)	10	20	20
Outside leg K_t	2.24	3.32	3.96
Second leg K_t	1.85	2.71	2.82
Inside leg K_t	1.84	2.59	2.63

the mechanical motion and including some symmetry. Messenger shows good correlation with steady-state results between FEA and experimental data. It was therefore determined that this FEA model could be used to determine the adequacy of the current work. Three sample cases were run with the geometries listed in Table 2.9. It is of interest to note that the FEM takes approximately 45 minutes to run a simulation, whereas the FDM runs in seconds (generally under a minute, depending on convergence). Results from the first two cases are shown in Figures 2.13 and 2.14. These figures show the comparison of the FDM to the FEM for outside and inside legs. The results of the second legs displayed similar results to those of the inside legs. A linear interpolation of the FEM data along the legs was used to calculate the percent maximum and mean errors in temperature rise of the FDM compared to the FEM. These errors are presented in Table 2.10. Figures 2.13, 2.14, and 2.15 show that for greater temperature differences between the outside and the inside legs the error of the outside K_t value increases. This is believed to be due to the constant temperature approximation across the array that was used in the formulation of the K_t values. However, the adequacy of this approximation is shown in that in the three cases presented here the maximum error in temperature rise in any case is only approximately 5.3% as shown in Table 2.10.

Case three was chosen for comparison with other simplification methods. This design was chosen because of the significant differences in the K_t values between the outside and inside structures. Case three was run with the K_t values presented in Table 2.9, a K_t

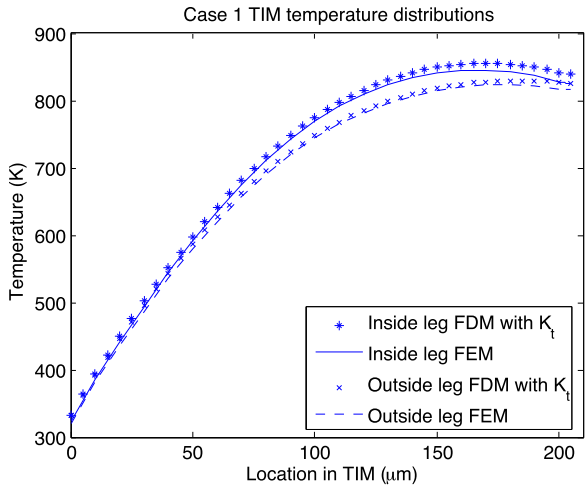

Figure 2.13: Comparison of FDM and FEM for case 1

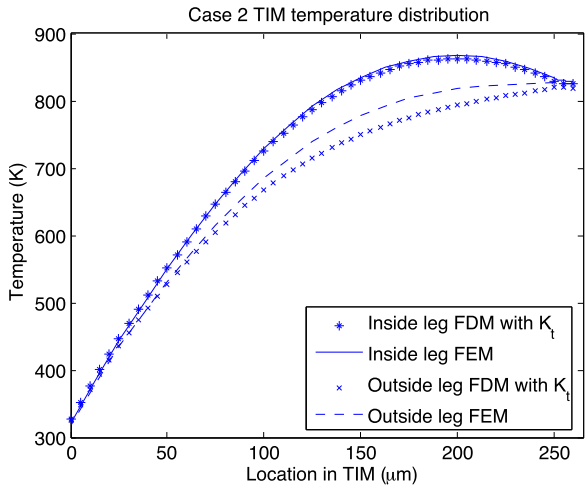

Figure 2.14: Comparison of FDM and FEM for case 2

equal to one for the entire model, and K_t values calculated using the formulas for F_s in [8] (i.e. 4.5 for the leg nodes and approximately 2.6 for the shuttle). As shown in Table 2.10 and Figure 2.15, the K_t values generated in this work show a significant improvement over either of these other two simplifications.

2.6 Conclusions

In conclusion, it has been shown that high accuracy and significant reduction in computational expense, by reduced order modeling, can be achieved in the thermal anal-

Table 2.10: Mean and max percent error in temperature rise between FEM and FDM for all cases

	% Error	Outside	Second	Inside
Case 1	Max	3.4	3.1	2.9
	Mean	1.1	2.0	1.2
Case 2	Max	3.6	1.9	1.6
	Mean	2.1	0.9	0.5
Case 3	Max	5.0	5.3	5.2
	Mean	2.3	1.5	0.9
Other simplifications methods (Case 3)				
$K_t = 1$	Max	47.6	42.3	41.9
	Mean	32.8	28.0	26.8
F_s from [12]	Max	15.5	17.6	18.7
	Mean	9.6	12.6	13.4

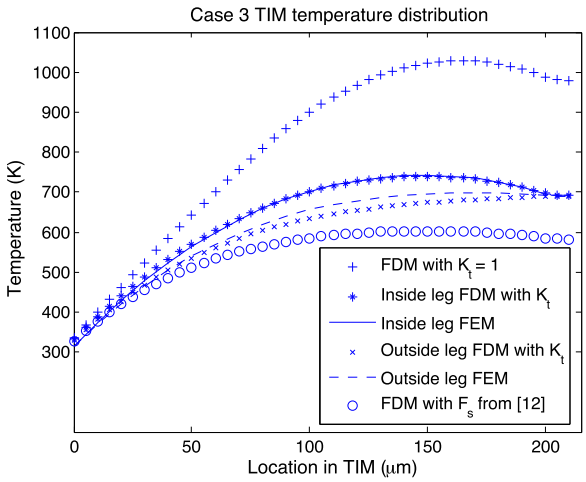

Figure 2.15: Comparison of FDM with various K_t values and FEM for Case 3

ysis of lineshape microstructure arrays by use of the K_t value developed in this work. An equation to calculate these values based on structure and array geometries has been developed using the average air temperature below the structure to calculate the temperature-dependent thermal conductivity of air. It was also shown that due to the nature of microstructure arrays, structure position in the array influences the heat losses and thus the K_t values. Therefore, different coefficients were developed to represent outer, second, and inner structures in an array. It has also been shown that the error in the fit developed was within an acceptable range. Additionally, it was shown that the model developed can be

used for single structures as well as arrays by setting the g_h spacing at an appropriate value. Finally, implementation of the K_t value was demonstrated for the analysis of systems such as the thermomechanical in-plane microactuator (TIM), with superior results to previous simplification methods.

2.7 Acknowledgments

This material is based upon work supported in part by the National Science Foundation under Grant No. 0428532. This work has also been submitted for review in [24].

Chapter 3

Calibration Approach for Thermomechanical In-plane Microactuator Self-sensing

3.1 Abstract

Microelectromecahanical system (MEMS) actuation is a growing area of research. One obstacle for use of actuation in MEMS applications is the difficulty of proper sensing. Recent work has been done that shows the potential for thermomechanical in-plane microactuators (TIMs) to act as self-sensors by using the piezoresistive characteristic of silicon. However, to implement this technology a calibration method needs to be devised to account for variations between TIMs. This work presents an approach for this calibration consisting of two parts that compensate for variation in fabrication and material properties. Test structures are presented that will enable this calibration to be done on-chip, and validation is given for the usability of this approach. Two validation approaches are used. For the first approach, data previously gathered was analyzed using the TIM itself for calibration. This approach showed significant correlation with the model; however, this approach confounds any sensing signal and therefore was used only for general model validation. The second approach uses a novel calibration structure that decouples the mechanical and electrical characteristics. This approach showed correlation with test data within the bounds of experimental uncertainty in nearly all cases. Suggestions are given concerning implementation.

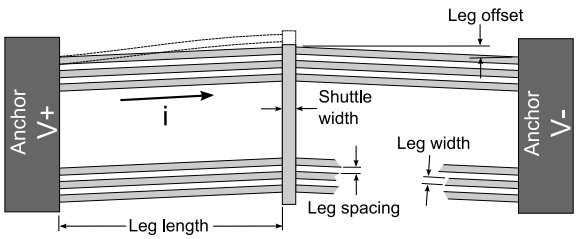

Figure 3.1: Schematic of thermomechanical in-plane microactuator (TIM).

3.2 Introduction

Study of microelectromechanical system (MEMS) actuation has become a major area of research [1], [13], [19], [25]–[28]. Thermomechanical in-plane microactuators (TIMs), as seen in Figure 3.1, have shown advantages in relatively high force and displacement abilities [17], [29]. Recent work by Waterfall et al. has shown that the piezoresistive property of silicon [5] shows promise in allowing the varying stress-states of the TIM, due to actuation, to enable the TIM to act as a self-sensor [4]. One major obstacle to the implementation of TIM self-sensing is device-to-device variation. This variation includes geometry and material property variability between devices due to concerns such as processing and doping level variations. To perform adequate self-sensing of the TIM, it is essential to determine a calibration approach for TIM modeling. This paper will present a two-step approach for calibration of the TIM. Results of this approach will be given, including validation testing. Finally, conclusions will be given on the efficacy of the proposed calibration approach.

3.3 Calibration approach

As previously mentioned, there are two primary areas of variation in the fabrication of TIMs: manufacturing variation (dimensional variation), caused by the difference in undercutting during the etching process of fabrication; and material property variation, caused by grain size and orientation, as well as dopant levels variations.

3.3.1 Manufacturing variations

Manufacturing variation, or dimensional deviation from the mask layout, is caused by undercutting of the mask during the etching process of fabrication. This difference in geometry significantly changes results in the thermophysical modeling of the TIM. This line width of the legs of the TIM affects resistance (thermal and electrical), and heat transfer, as well as the mechanical motion. Therefore dimension determination is essential for proper characterization of the TIM.

One proposed method for line width determination is described by Buehler et al. using a van der Pauw test structure and a bridge structure [30]. In this way an accurate measurement of the fabrication line width can be obtained ($\pm$ 0.1 μm). This approach allows for all measurements to be done electrically on-chip. However, the bridge structure was not available for this study, so line width measurements were taken visually using scanning electron microscopy (SEM), or optical microscopy.

3.3.2 Material properties

Along with correction of the geometric dimension of the TIM, calibration needs to be performed for correction of the material properties. Material properties of concern include the coefficient of thermal expansion (CTE), thermal conductivity, and resistivity. It is assumed that Poisson's ratio and density do not vary significantly [11]. Calibration of material properties for this particular application present two main concerns: temperature dependence and on-chip viability. Due to the extreme temperature variation experienced by the TIM, it is essential to know the temperature dependence of the properties in question. Also, for the viability of using the TIM as a self-sensing actuator, a simple on-chip approach to calibration is desired.

The approach of this work was to use published material properties for CTE [31] and thermal conductivity [11], and to calibrate resistivity. Work was done to explore the possibility of using the TIM itself as a calibrator; these results will be presented later. However, it was determined that this approach confounded piezoresistive changes in resistance with temperature changes in resistance. This approach was used in this paper to show the

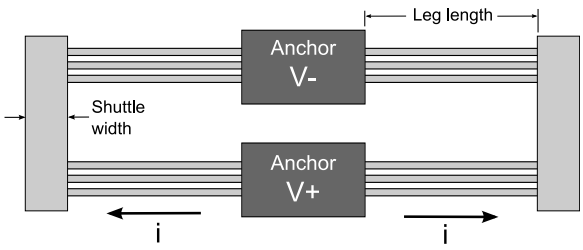

Figure 3.2: Schematic of thermal dependent resistivity calibration mechanism (TDRCS).

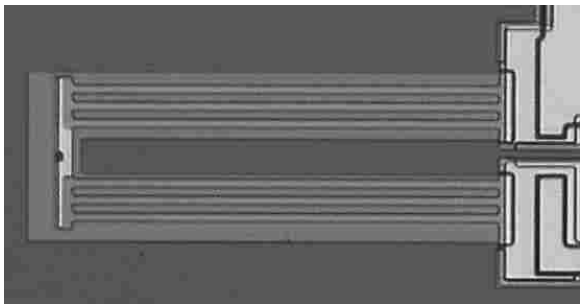

Figure 3.3: Optical microscope imaging of half of the TDRCS.

ability of the calibration approach, but would be unable to be incorporated for the final self-sensing model. Due to this phenomena, the temperature-dependent resistivity calibration structure (TDRCS) seen in Figures 3.2 and 3.3 was designed to decouple these effects. This structure allows a representation of the geometries of the TIM for electrical and thermal changes, without the mechanical stresses (and thus piezoresistive changes) in the TIM setup. The TDRCS operates by inducing a current through the mechanism and measuring the voltage drop. The current is applied at several levels in the operational range of the TIM (ensuring the TIM stays below 800 K where radiation begins to become an issue [11] and much below the point where self-annealing occurs at 1073 K [17]). From this data a power-resistance curve can be created. This power-resistance data can then be used to calibrate the TIM model; this implementation will be explained later. It is important to note that this approach does not give a pure resistivity measurement in that other variations can be convoluted into this change in resistance. However, this allows the model to account for changes in other properties through one calibration.

Table 3.1: Dimensions for model validation using unloaded TIM data

Parameter	Value
Leg length	250 μm
Leg offset	5.5 μm
Leg width (including undercut)	2.5 μm
Leg spacing (including undercut)	3.5 μm
Leg thickness	3.5 μm
Number of legs	4

3.4 Results

Several different tests were performed to implement the calibration technique presented in this work. Initial testing was done to gather the calibration data needed, as discussed earlier. All test mechanisms were fabricated using the MUMPs fabrication process [22].

3.4.1 Manufacturing variation results

For this work, visual imaging was used to determine the undercut that occurred during the fabrication process. SEM images were used to measure the actual line width for the particular die used. It was determined that the TDRCS and TIM had insignificant undercut on the chip used in this testing (this is not always the case in that undercutting has been seen repeatedly in other situations). Data previously gathered was also analyzed in this work. Undercut was determined using an optical microscope to be approximately 0.25 μm for these earlier devices.

3.4.2 Power-resistance data

Two different approaches for obtaining the power-resistance (P-R) data necessary for resistivity calibration are given in this paper. First, a simple approach was used where, for an unloaded TIM, voltages were measured at various current levels. Data for this approach was gathered for a previous study and was adapted to this work. Parameter values for this TIM are given in Table 3.1. Using this previous data a P-R curve was generated as

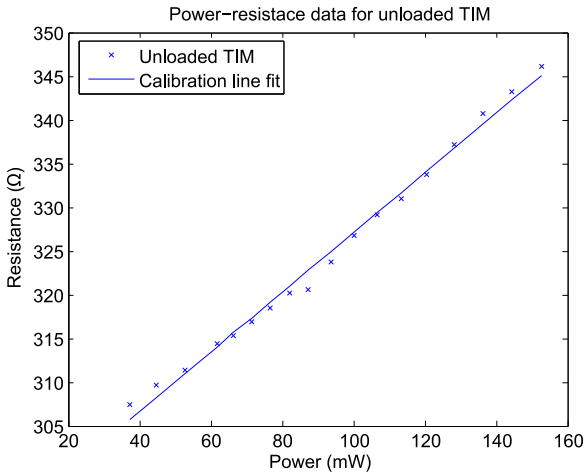

Figure 3.4: Power-resistance plot for unloaded TIM, with an approximate maximum current and voltage of 18 mA and 6 V.

Table 3.2: TIM and TDRCS dimensions for model validation

Parameter	Value
Leg length	150 μm
Leg offset (TIM only)	2.62 μm
Leg width (including undercut)	3 μm
Leg spacing (including undercut)	7 μm
Leg thickness	3.5 μm
Number of legs	3

seen in Figure 3.4. The slope of the line fit for the data was calculated to be approximately 0.341 Ω/mW. This slope was then used in the calibration model which will be explained later.

The second approach for obtaining the P-R data was to use the TDRCS. Parameter values for the TDRCS and corresponding TIM are presented in Table 3.2. (It is important to note that these two approaches were performed on TIMs from different MUMPs process runs and with different geometries and number of legs.) Four-point probe testing was used to induce a current through the TDRCS and measure the voltage drop. To determine an appropriate operating range, a preliminary thermal analysis was performed. A maximum current of 15 mA was used (approximately 4 V), this ultimately corresponded to a maximum temperature of only 500 K. The power dissipated at this current should generally

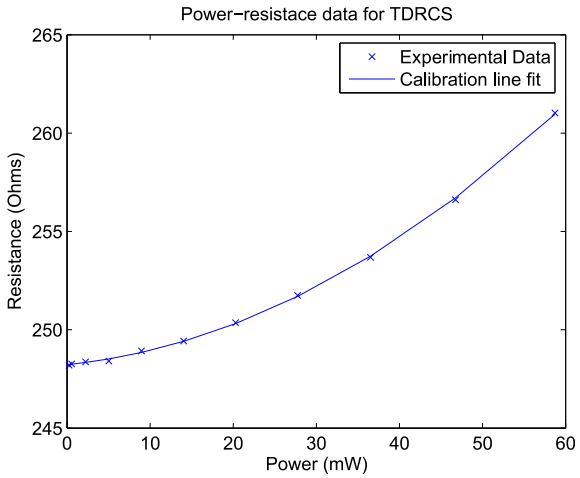

Figure 3.5: Power-resistance plot for TDRCS, with an approximate maximum current and voltage of 15 mA and 4 V.

correspond to the maximum power dissipation expected in the TIM. Using several current levels up to this maximum, a P-R relationship was obtained as seen in Figure 3.5. It is important to note that the TDRCS experiences a "burn-in" period, in that until the maximum current is reached the device displayed non-uniform results. The exact cause of this "burn-in" phenomena is unknown, but has been repeatably observed on multiple devices (TIM and TDRCS). This could be due to micro-annealing, but this is considered unlikely due to the relatively low temperatures experienced. It also may be attributed to some residual material from the fabrication or release processes that is burnt off as the TIM heats up. Regardless of the source, once the maximum operating voltage was reached, repeatable measurements were obtained for each run afterward. Therefore the first current applied is the max current after which randomization was used. A quadratic fit was used, and was found to be

$$\Delta R = 2.97 \cdot 10^{-3} P^2 + 4.27 \cdot 10^{-2} P \tag{3.1}$$

where P is power in mW and ΔR is in Ω. The intercept will be set for each individual TIM.

3.4.3 Physics model

A model describing the physics of the TIM was developed to calculate the temperature profile, stresses, force and displacement outputs, and P-R data for the TIM. This model consists of two main components: a finite difference model for temperature profile determination, and a finite element model for stress, force, and displacement determination. An expanded one-dimensional finite difference approach was used. This model accounted for heat transfer down each leg of the TIM as well as heat transfer down the shuttle. Heat loss to the substrate at each point was calculated using a representative thermal resistance of the air between the leg and substrate and a thermal correction technique described in Chapter 2 [24]. This approach is based on the finite difference equation,

$$\begin{aligned} K_t\left(\frac{T_i - T_s}{R_t \Delta x}\right) - I^2 \frac{R_e}{\Delta V} &= \kappa_i \left(\frac{T_{i+1} - 2T_i + T_{i-1}}{(\Delta x)^2}\right) \\ &+ \left(\frac{\kappa_{i+1} - \kappa_{i-1}}{2\Delta x}\right)\left(\frac{T_{i+1} - T_{i-1}}{2\Delta x}\right) \end{aligned} \tag{3.2}$$

where K_t is the thermal correction value mentioned previously, T is element temperature and T_s the substrate temperature, R_t is the thermal resistance of the air below the element, I is electrical current, R_e is the electrical resistance of the element, ΔV is the differential volume, κ is the thermal conductivity, Δx is the element length, and the subscripts $i+1$, i, and $i-1$ denote the next, current, and previous elements respectively. One complication with this approach is that many material properties are dependent on temperature. To allow for temperature dependence of material properties, an iterative approach was used basing the material properties of the current iteration on the temperature profile of the previous iteration. This iterative approach was run until the temperature profile converged. This model exploited the symmetry that is inherent in the TIM design to reduce computation, by using insulated boundary conditions to represent the lines of symmetry. Shuttle nodes incorporated an extra conduction term to account for heat transfer from the legs, and thermal correction values of one to account for an approximation of the heat transfer characteristics.

The end node of the shuttle used a thermal correction value with a theoretical zero value for the horizontal gap.

Once a temperature profile was created for a given current, this profile was input into a finite element model (FEM) as body forces. Using ANSYS, a commercially available FEM package, force-displacement pairs were gathered. First, the TIM was allowed to expand fully (unloaded). This maximum displacement was determined, and displacements were then applied to the front end of the TIM in set increments to represent different loading conditions. This was repeated for various current levels.

Before use of this model, calibration of the geometries and material properties needed to be incorporated. A slightly altered version of this model was used to incorporate the calibration data obtained from the TIM and TDRCS approaches. In this altered model the mechanical aspects were removed because the mechanical motions of the system have little affect on the electrical and thermal material properties. The incorporation of the obtained P-R calibration slope was done by performing a simple optimization process to minimize the difference between the modeled curve of the P-R curve and the TDRCS P-R curve. For the TIM calibrated approach the temperature dependence of resistivity was assumed linear in the operating range and for the TDRCS calibrated data a quadratic fit was used. By inputing a nominal resistance from an actual TIM, the optimization routine needed only to change the coefficients of the temperature-resistivity curve until the output power-resistance curve and the calibration curve were equal. This calibration for temperature-dependent resistivity for the unloaded TIM produced a slope of approximately 2.8 Ω·m/K, while the TDRCS quadratic calibration produced coefficients of $1.96 \cdot 10^{-2}$ Ω·m/K^2 and $1.16 \cdot 10^{-5}$ Ω·m/K.

3.5 Validation

For this work validation testing will be reported in two parts: first, validation for the physics model based on the calibration data of the unloaded TIM calibration approach; second, validation for the physics model based on the TDRCS approach. Each validation will be presented with a discussion of the results and limitations.

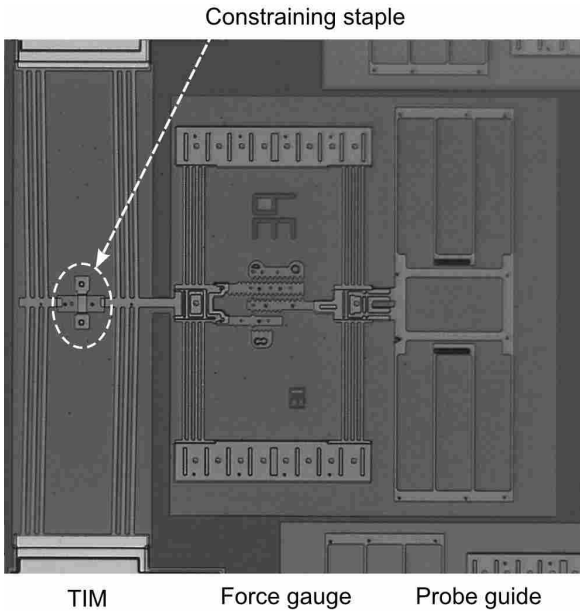

Figure 3.6: Experimental setup for calibration validation.

3.5.1 Unloaded TIM calibration validation

For validation of calibration using an unloaded TIM, force and displacement data gathered previously for another work was used. The maximum current and voltage used for the current work were approximately 18 mA and 6.1 V respectively. The forces were adjusted for undercut and to be consistent with the Young's Modulus used in this work. Dimensions used were given previously in Table 3.1. This model was run at various current levels. The ANSYS model used in this validation was a 2D analysis using BEAM3 elements. This was done because any out-of-plane buckling that may have occurred when the TIM was loaded, was constrained by a staple similar to the one seen in Figure 3.6. The calibrated model and original data for the current levels examined are presented in Figure 3.7. The error bars represent ± 0.25 μm and approximately ± 7.5 μN, or the uncertainty in the optical vernier used for displacement and force measurements. This represents a conservative value of the error in measurement, but is not a reflection on the repeatability of the TIM (for more information on TIM displacement and force repeatability see [32] and [33]). At the higher currents different buckling modes were experienced due to a violation of the

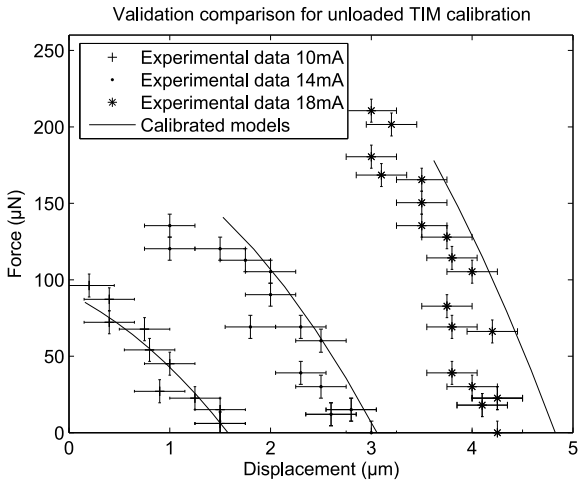

Figure 3.7: Calibrated model validation for unloaded TIM calibration approach

slenderness ratio discussed by Wittwer [34]; therefore the higher current levels were not explored in this work.

3.5.2 TDRCS calibration validation

For validation of calibration using the TDRCS, the acquired resistivity data was input into the full model. This model was run for three current levels in the experimental range. A 3D BEAM4 ANSYS model was used for this validation. This was done because the constraining staple that was used previously was not incorporated into this design. This allowed for out of plane deflections when the TIM was loaded. Modifications were made to the boundary conditions of the model to simulate the non-ideal boundary conditions in the anchors of the actual test structure.

Experimental testing was performed on a MUMPs fabricated TIM from the same die as the TDRCS. The setup for this device consisted of the TIM, a force gauge [35] with an optical vernier, and a probe guide as seen in Figure 2.1, although the TIM in testing was not constrained by a staple as already mentioned. The force gauge was analyzed using the same Young's Modulus as that for the TIM model (adjustments for undercut would also have been incorporated had any been measured for this device). The dimensions of the TIM and TDRCS were given previously in Table 3.2. Gold was deposited on parts of the

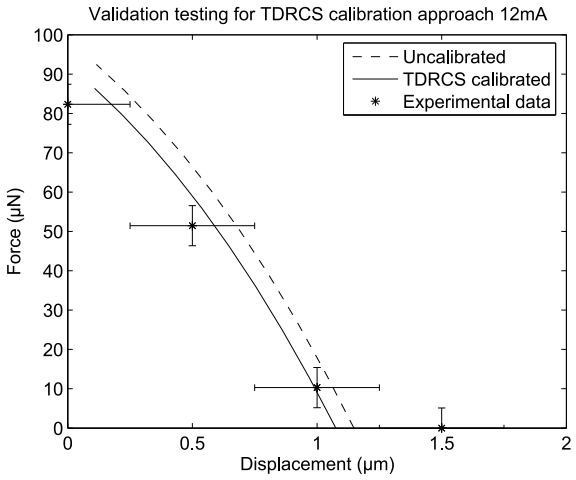

Figure 3.8: Calibrated model validation for TDRCS calibration approach with $I = 12$ mA

TDRCS shuttle to reduce electrical resistance, and better represent the TIM. The vernier had displacement resolution of 0.5 μm, and force resolution of approximately 10.3 μN. The error bars represent ± 0.25 μm and ± 5.1 μN, or the approximate uncertainty of the vernier.

At each given current level, forces were applied with a micro probe to attain the desired force or displacement output from the TIM. Maximum current and voltage in the TIM were 14.999 ± 0.014 mA and 3.7079 ± 0.0021 V respectively. In this setup, the probe guide is fixed to ground and any displacement of the TIM is resisted by the stiffness of the probe guide and force gauge. To obtain an unloaded reading for the TIM, the probe guide was pulled backward until the force gauge read zero force. All other readings were done at given displacement levels. Displacement was incremented rather than force due to the resolution of the different readings. Experimental data with the model predictions, calibrated and uncalibrated, are given in Figure 3.8 through Figure 3.10. The uncalibrated model is based on the nominal resistance measured for the TIM and a quadratic approximation of temperature dependence of resistivity reported in [11]. If underetch had been detected a greater disparity would be seen between the uncalibrated and calibrated models.

It can be seen that the model matches the experimental data within the error of the vernier in almost all cases. At the unloaded position the error is slightly larger possibly

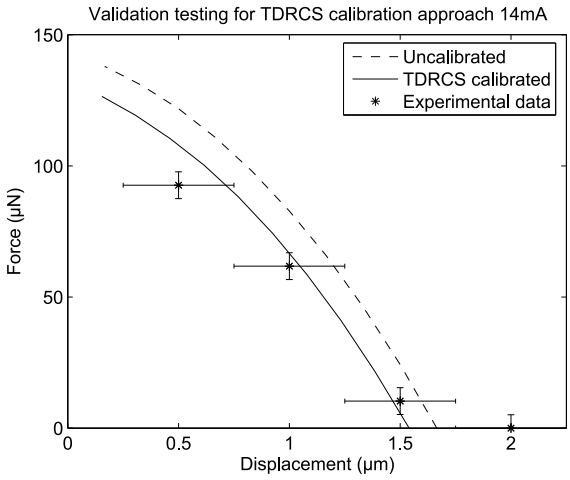

Figure 3.9: Calibrated model validation for TDRCS calibration approach with $I = 14$ mA

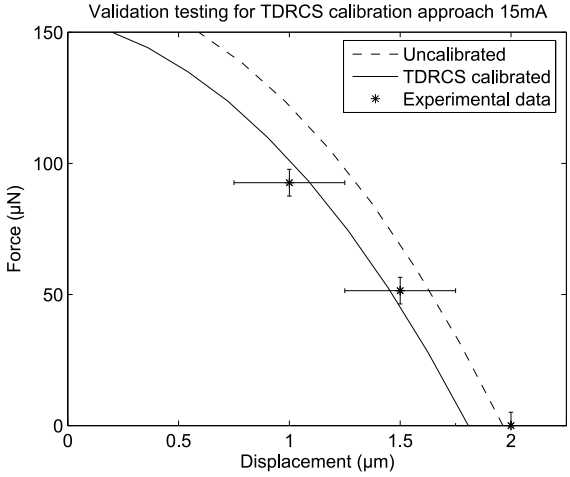

Figure 3.10: Calibrated model validation for TDRCS calibration approach with $I = 15$ mA

due in part to greater experimental measurement techniques (i.e. target force as opposed to target displacement); however, the deviation seen in the experimental data from its trend is not fully understood.

3.5.3 Validation discussion

The two types of validation presented in this paper show separate information about the calibration process presented. The first validation approach used unloaded TIM data to

obtain the temperature dependence of resistivity. This mechanism also experienced undercut during the fabrication process that was accounted for in calibration. When implemented into the full model, this approach showed close correlation with the experimental data at low currents, with slight deviation at higher current levels. This is believed to be in part caused by other buckling modes as described earlier, or from friction forces due to the staple. This approach, however, confounds the piezoresistive changes in the TIM due to the stresses in the actuated, unloaded position, with that of the temperature dependence of resistivity. Therefore, this approach is useful for showing the ability of the model to determine the TIM's behavior, but is inadequate for implementation for a self-sensing application.

The second type of validation presented used a novel structure, the TDRCS, to eliminate the confounding effect experienced with the first method. When this structure was used to calibrate the full model, the model showed good correlation with the experimental data. It can also been seen that with higher power input the discrepancy between the calibrated and uncalibrated models increases. This discrepancy has also been seen to be much greater in other TIM designs.

One suggestion for future use of the TDRCS is in the design of the shuttle. In this work, as was mentioned, gold was deposited on parts of the shuttle to reduce the electrical resistance of the shuttle but still simulate the heat transfer that would occur. However, at high currents the gold would begin to burn off (higher currents than used in this work, but still within the possible range of TIM operation). It is assumed that this was caused by the high current that would pass through the thin gold layer. It is suggested then that a wider center shuttle be used in the TDRCS than that in the TIM. This will not greatly change the heat transfer in the model, but will allow for a closer representation of the current flow in the shuttle. This will also allow for a greater range of calibration and therefore of actuation.

3.6 Conclusions

This work has developed a calibration technique to compensate for variations in fabrication and material properties of the thermomechanical in-plane microactuator (TIM). The two-part approach presented here calibrates a physics-based model of the TIM for these variations. Determining the underetching during the fabrication process in this study

was done using imaging of the devices; however, it is proposed that this would be done on-chip using well established line-width determination techniques, such as a van der Pauw and line width measurement structure.

The second phase of calibration is developing a temperature-dependent resistivity relationship. In this work this relationship is not a pure resistivity equation in that other variables are most likely confounded with the results. However, this allows for variations in other properties to be lumped into one calibration approach. This calibration was done using two different approaches. Both an unloaded TIM and a calibration structure (TDRCS) were used to obtain the temperature dependent resistivity data. Once this data was gathered, validation of this calibration approach was performed.

This validation showed through the unloaded TIM approach that the model was able to describe the output of the TIM at lower currents with slight deviations at higher currents. However, this approach confounded the piezoresistive effect of the TIM in the unloaded position. To eliminate this confounding, the TDRCS was developed. This allowed for calibration to be done without confounding the sensing signal with the calibration. This data shows that adequate calibration of the TIM is possible using the TRDCS. This calibration approach will allow the principle of self-sensing of the TIM to be possible by compensating for variations between devices.

3.7 Acknowledgment

This work was funded in part by DARPA through a subcontract with Block MEMS, LLC, and the National Science Foundation Grant No. 0428532. The authors would also like to acknowledge the help of colleagues in the Compliant Mechanisms Research Lab at Brigham Young University. This work will also appear in the Proceedings of the ASME 2008 International Design Engineering Technical Conferences (IDETC 2008) [36].

Chapter 4

Modeling and Calibration for Self-sensing of a Thermomechanical In-plane Microactuator

4.1 Abstract

Actuation and sensing is a crucial area of growth in the field of microelectromechanical systems (MEMS). One particular actuator that has shown promise in versatility and viability is the thermomechanical in-plane microactuator (TIM). Previous work has shown preliminary results that suggest by using the piezoresistive property of silicon, the TIM may be able to be used as a self-sensing actuator. This paper develops a multi-physics model of the TIM that allows the piezoresistive change in resistivity to be isolated from temperature-induced resistivity changes. This piezoresistive signal is then correlated to a given force-displacement output through modeled stress profiles of an actuated TIM. In this way the TIM is able to self-sense its mechanical outputs with no ancillary sensors. Calibration and testing have been performed on a single device with good correlation.

4.2 Introduction

As microsystems become more common, and sensing applications become broader, novel approaches to areas such as sensing and actuation become more important. In the field of microelectromechanical systems (MEMS), several types of actuation have been developed and analyzed [19], [25], [37]. Among these is the thermomechanical in-plane microactuator (TIM) [1], [12], [26], [29]. The TIM uses ohmic heating, thermal expansion, and geometric configurations to achieve its motion. As illustrated in Figure 4.1, as a current is induced in the thin legs of a TIM, ohmic heating occurs in the legs. This heating causes

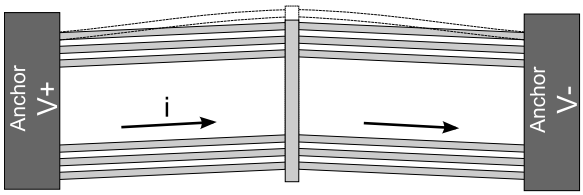

Figure 4.1: Thermomechanical In-plane Microactuator (TIM).

an expansion of the legs which, due to the geometric symmetry of the TIM, causes buckling of the legs and a forward motion of the center shuttle.

In order for MEMS actuators like the TIM to be viable on-chip devices, precise approaches to force and displacement sensing are required. One current area of sensing operates on the principle of piezoresistance. Smith first reported the piezoresistive property of silicon in 1954 [5]. Recent work has shown the possibilities of using structures in stressed states as sensing devices where the entire structure is a sensing member, rather than a selectively-doped portion of the device [6], [7]. Work done by Messenger has shown high accuracy for displacement sensing of the TIM using this principle [3]. However, these approaches have required ancillary sensors which increase the footprint of the TIM, as well as requiring separate actuation and sensing signals. Recent work presented by Waterfall et al. [4] has shown that during actuation of the TIM there is a measurable piezoresistive effect which correlates to the mechanical outputs of the TIM. Waterfall et al. proposes that this signal would enable the TIM to operate as a self-sensing actuator, or in other words by sensing the electrical state of the TIM, the mechanical outputs could be obtained without any ancillary sensors. This could effectively reduce the footprint of the device and allow the actuation and sensing to be coupled in one electrical signal.

This paper presents work that develops an approach for the self-sensing of the TIM. The approach is based on a multi-physics model of the TIM's behavior. Essential to the efficacy of this approach is the development of a calibration method. An earlier approach to calibration proposed using a secondary calibration structure [36] for calibration of the electrical resistivity; however, an alternative calibration approach that calibrates solely using the TIM will be presented here. This calibration allows for accurate prediction of the force-displacement curve of the TIM for a given electrical input. Sensing is incorporated

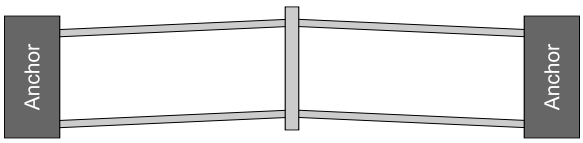

Figure 4.2: Schematic of “one leg” TIM.

into the model by using the measured piezoresistive effect to detect both displacement and force outputs of the TIM. This approach, as well as an approach for calibration of the sensing, will be presented. Validation testing results are shown comparing the model prediction with measured test data with good correlation. A discussion of the results and future research and implementation is given. Finally, conclusions will be presented.

4.3 Physics-based model

To allow the TIM to operate as a self-sensing actuator, proper characterization of the physics of the TIM is needed. This section describes a physics-based model of the TIM behavior. For simplicity in modeling a “one leg” TIM was used for modeling and testing as seen in Figure 4.2. This model begins with an electrothermal model to predict a temperature profile of the TIM. These temperatures are then used as inputs into a mechanical model which determines the mechanical outputs caused by the thermal expansion and buckling of the legs. Both of these models are highly dependent on material and geometry variation. A calibration approach was developed to account for this variation, a description of which will be given later. Many of the material properties used in these models are temperature-dependent. Temperature-dependent properties used included the thermal coefficient of expansion (CTE) [31], thermal conductivity of air [38], and the thermal conductivity of polycrystalline silicon [11]. A fourth-order fit was used for the CTE, whereas a third-order fit was used for the thermal conductivities. Material properties that were approximated as temperature-independent were Young’s Modulus and Poisson ratio [11].

4.3.1 Thermal modeling

Thermal modeling of the TIM was done using a finite difference model (FDM), created in MATLAB. The governing heat transfer equation is

$$\frac{\partial}{\partial x}\left(\kappa\frac{\partial T}{\partial x}\right) = -q_{gen} + q_{loss} \tag{4.1}$$

where x is the position along the leg, T is the temperature, q_{gen} is the heat generation, and q_{loss} is the heat loss. Using the finite difference approach Equation 4.1 becomes

$$\kappa_i\left(\frac{T_{i+1}-2T_i+T_{i-1}}{(\Delta x)^2}\right)+\left(\frac{\kappa_{i+1}-\kappa_{i-1}}{2\Delta x}\right)\left(\frac{T_{i+1}-T_{i-1}}{2\Delta x}\right) = -I^2\frac{R_e}{\Delta V}+K_t\left(\frac{T_i-T_s}{R_t\Delta x}\right) \tag{4.2}$$

where T is the temperature at a node; x is the location along the leg; κ is the temperature-dependent thermal conductivity; I is the electrical current in the beam; R_e is the electrical resistance associated with the node; K_t is a thermal correction value that allows for reduced order modeling by compensating for heat loss not directly out the bottom of the beam [24]; R_t is the thermal resistance directly out of the bottom of the beam to the substrate; and subscripts $i-1$, i, and $i+1$ are the previous, current, and next nodes respectively.

Using symmetry to reduce the computational power required, the TIM legs and shuttle were discretized and a steady-state analysis was performed. An iterative approach was necessary due to the temperature dependence of many of the material properties. This was done by determining the current temperature-dependent material property values based on the temperatures of the previous iteration. This was repeated until the temperature profile converged. In this way a temperature profile for the leg of the TIM was attained.

4.3.2 Mechanical modeling

The temperature profile generated by the FDM was then used as input into a mechanical finite element model (FEM), using ANSYS. A 3D beam element (BEAM4) was used. This element allowed temperature inputs as body loads. It also allowed for out-

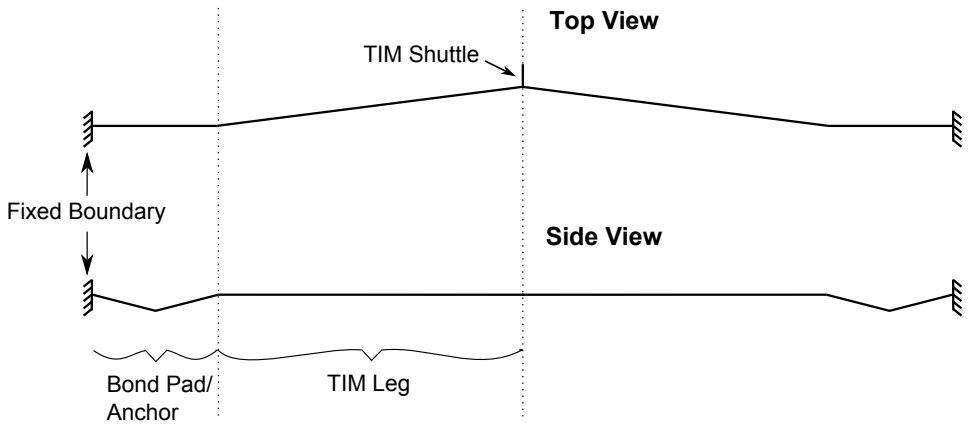

Figure 4.3: Schematic of ANSYS BEAM4 model.

of-plane deflections for more precise modeling. Additional beam elements were added to the ends of the leg to account for the minor non-planar nature inherent in the anchor due to conformity of the polysilicon layers, as well as allow for other non-idealized boundary conditions. The other edge of the anchor had fixed boundary conditions (see Figure 4.3).

Once the temperature profile was input into the model, ANSYS determined the static position of the TIM based on thermal expansion and buckling of the TIM legs. This position corresponded to a mechanically unloaded, yet actuated, TIM. This unloaded, or zero output-force, condition gave the greatest displacement the TIM would achieve at the given actuation current. Incremented displacements between the fabricated and unloaded positions were then applied to the end of the TIM shuttle and reaction forces were recorded. In this manner a unique force-displacement curve was generated for a given actuation current. A given current level can be approximated as an unchanging temperature profile, regardless of loading [39]. It is important to note that the FEM only modeled one grouping of the TIM's legs (a half model), so the output forces from the ANSYS model were doubled to accurately model an actual TIM. The displacements, however, would be the same in a half or full model.

In addition to the force-displacement data output, the axial stress profiles of the mechanical model were also output for each displacement. This information will be used later in the piezoresistive model.

4.3.3 Calibration overview

One of the major obstacles in accurate modeling of the TIM is the device-to-device variation. Specifically the resistivity and piezoresistivity coefficients are expected to vary between runs. Work by the authors was done to develop an approach to account for this variation in the TIM [36]. This method posed certain challenges in that it required a different calibrating structure which caused complications in proper correlation between the model of the calibrating structure and the TIM. In this work, this concept was adapted to use a TIM as its own calibrating structure with an iterative calibration approach to determine electrical resistivity and piezoresistivity. All other material properties were determined from documentation as mentioned previously.

In addition to variation in material properties, geometric variation was also found to affect TIM behavior. Geometric variation was considered to be the difference between the designed dimensions and the actual final fabricated form. This variation was determined optically. However, when implemented on-chip this may be done using structures such as a Van der Pauw and and bridge structures [30] depending on the precision needed.

Once the dimensional corrections were made calibration of the electrical resistivity could be done. This process will be explained in detail later.

4.4 Sensing approach

The physics-based model described in the previous section is designed to determine the thermal and electrical states of the TIM without regard to the piezoresistive effect. The resistance calculated in the model can then be compared to the actual measure resistance. The difference between these two values is the sensing output and will correspond to a particular force-displacement output.

4.4.1 Piezoresistive model

The piezoresistive model that was used for this study was developed by Messenger [3]. His work shows validation testing for such an approach. In this approach a stressed beam is discretized and the axial and maximum bending stresses are determined for each

element. It was found that the piezoresistive change caused by pure axial loading exhibited a linear change in resistance, whereas stresses due to bending exhibited a quadratic effect (similar findings are reported in [40], [41]). Therefore a piezoresistive coefficient (π coefficient) was determined for pure tensile stresses, and a separate π coefficient was determined for bending stresses squared. Due to the quadratic nature of bending effects on piezoresistance, at low stress states the linear term from axial stress dominates. A simple check was performed using the model developed in this work to determine if bending stresses would contribute a significant portion of the piezoresistive signal. To accomplish this the stress profiles of the highest actuation current reported in this work were obtained. Using piezoresistive coefficients reported by Messenger [3] it was determined that for the unloaded case (maximum bending scenario), the piezoresistive contribution of bending was only 0.31%, and that at a zero displacement loading condition that contribution was 0.000001%. It is important to note that these coefficients were determined at room temperature and do not account for any temperature dependence, but it is assumed that similar changes would occur in both coefficients and similar findings would result when compensated for temperature effects. Therefore the piezoresistive effects due to axial stress were dominant, and the effects due to bending were ignored.

4.4.2 Modeling approach

To incorporate sensing into the model, it was necessary to isolate the resistances where the stress was calculated. This is essential because the piezoresistive model operates on a fractional percent change in resistance. That is, a beam with a given stress distribution will change resistance by a certain fraction of its nominal resistance. In this model of the TIM the stress is gathered only for the legs, not for the shuttle. Therefore the shuttle resistance was taken out before applying the piezoresistive change, and then reapplied for comparison with the measured data.

Implementation of this model was done in a table look-up approach. The input for the model was the measured voltages at a given current. This was compared to the voltage change that occurred from temperature effects alone at that current. The difference between these two is assumed to result from the piezoresistive effect. The physics-based

model previously described predicts output force, displacement, stress profile of the TIM. By determining the piezoresistive change that would occur due to each stress profile, this voltage change can be correlated with a force-displacement pair. Therefore, by measuring the voltage change, the force-displacement outputs of the TIM can be determined. For values that do not lie on one of the calculated points, linear interpolation can be performed. By including more modeled points in the table, interpolation accuracy can be increased.

4.4.3 Temperature-dependent piezoresistance

To be able to use the piezoresistive effect as a sensing signal for the TIM, a basic understanding of the effect that temperature has on this piezoresistance is necessary. Various studies have looked at this property for single and polycrystalline silicon [42]–[45]. These have shown a general decrease in piezoresistive response for higher temperatures. They have also shown that increased dopant concentration decreases the temperature dependence. In [46] this general decrease in response for increased temperature is also shown; however, for high dopant concentrations ($\sim 10^{20}$ cm^{-3}) there is shown an increase in piezoresistive response for single crystal silicon. However, the temperature range is much lower than the range needed for this study. In none of the studies examined did the dopant type and concentration, the temperature range, and the crystalline structure match the current work. Therefore, in order to have data for a greater temperature range, correct dopant concentration, and proper crystalline structure, general temperature testing was done in-lab. The main objective of this testing was to understand the general trend of the piezoresistive effect with temperature.

A MUMPs-fabricated device like the one used by Johns et al. [6] was used to apply axial stresses in a beam and measure the piezoresistive response. A schematic of the device is given in Figure 4.4. This device was placed on a thermal stage in a vacuum chamber. Testing was performed from 300 K to 600 K using a K-20 temperature controller from MMR technologies. In order to extract the π coefficients from the test structure a resistivity using the measured resistance and the geometries was first attained. This was done so that the added resistance in the connecting crossbar could be subtracted and a fractional change in resistance of the legs could be determined. At each temperature setting different force

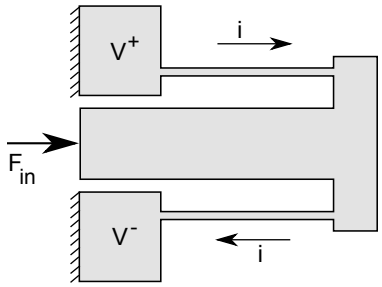

Figure 4.4: Schematic of structure used for piezoresistive coefficient determination.

loadings were applied using a microprobe, probe guide, and force gauge with an optical vernier much like those used in the TIM testing presented later (see Figure 4.8). With a known spring constant of the force gauge a force reading can be obtained by measuring the deflection. During fabrication of these devices there is often deviation from the design caused by underetching of the mask. For this run an underetch of 0.26 was measured on a particular device using a scanning electron micrograph; for simplicity a value of 0.25 was used to correct for the dimensioning of these devices and the determination of the spring constant of the force gauge.

The data gathered is shown in Figure 4.5 and is presented in two sets. The first set of data is calculated π coefficients at the temperature setting for each run. The second set of data presented in Figure 4.5 is the average π coefficient value at that temperature setting, with one exception. At 600 K the last run taken showed negligible piezoresistive effect unlike the other two runs at that temperature. This was considered an anomaly and, therefore, only the first two points are used to obtain the average coefficient at 600 K.

The main purpose of this experiment was to determine the general trend of the temperature dependence of the π coefficients. From the data gathered it was determined that the axial coefficients can be approximated with a negative linear relationship with temperature. This increase in piezoresistive signal at higher temperatures may be due to the high dopant concentrations of the MUMPs process and correspond to the slight increase reported by [46] in the lower temperature region. While this test establishes the expected trend for this work, fabrication variations are likely to introduce variability in both the

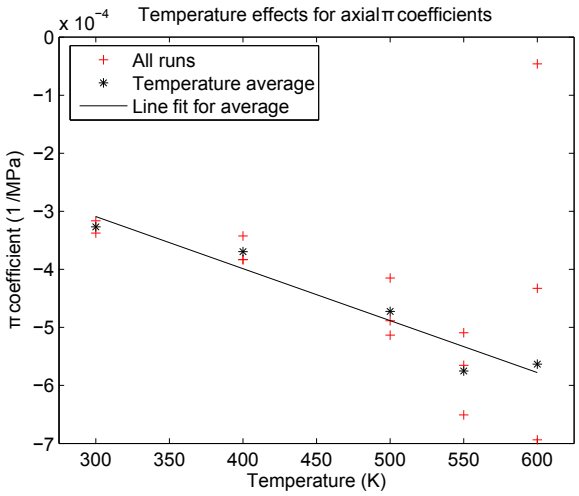

Figure 4.5: Temperature-dependent piezoresistive data.

room-temperature π coefficient and in its variation with temperature. Therefore, a calibration approach is proposed and validated in the next sections.

4.5 Iterative calibration approach for resistivity and piezoresistance

The calibration approach presented in this work is an iterative approach. A general process diagram for the calibration process is shown in Figure 4.6. Two material properties needed to be calibrated. The first is the temperature-dependent electrical resistivity which can be written

$$\rho = \rho_0 \left(1 + \alpha_1 (T - T_0) + \alpha_2 (T - T_0)^2\right) \tag{4.3}$$

where ρ_0 is the room temperature resistivity, α_1 and α_2 are temperature coefficients of resistivity, T is the current temperature, and T_0 is the ambient temperature. Four different data sets are needed in this approach. These are depicted in Figure 4.7, and a explanation of each will be given. The room temperature resistivity can be calculated using a measured nominal resistance (see Figure 4.7) and the specific designed geometries (corrected for underetch) as

$$\rho_0 = R\frac{A}{l} \tag{4.4}$$

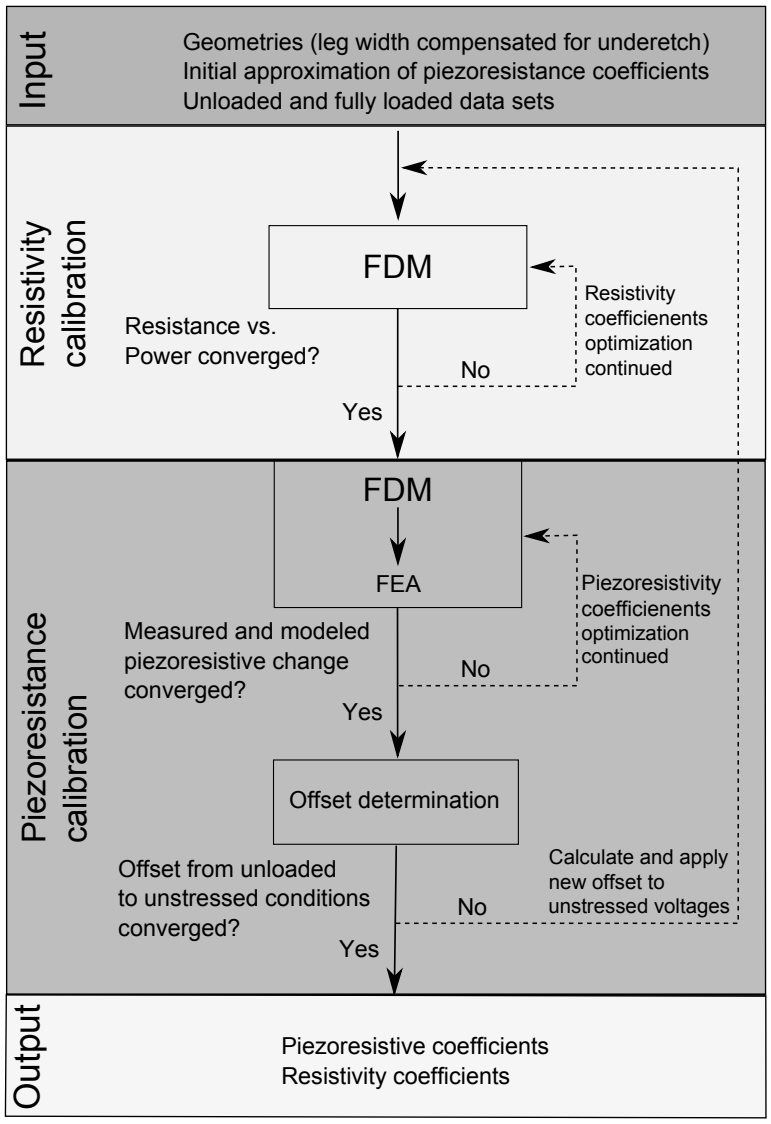

Figure 4.6: Process diagram of calibration approach.

where R is the resistance of the leg, A is the cross-sectional area of the leg, and l is the length of the leg. The second material property that needs to be calibrated is the temperature-dependent piezoresistance which can be written

$$\pi = \pi_0 \left(1 + \beta \left(T - T_0\right)\right) \tag{4.5}$$

where π is the temperature-dependent piezoresistive coefficient, π_0 is the ambient temperature piezoresistive value, and β is the temperature-dependent constant. Hence, the

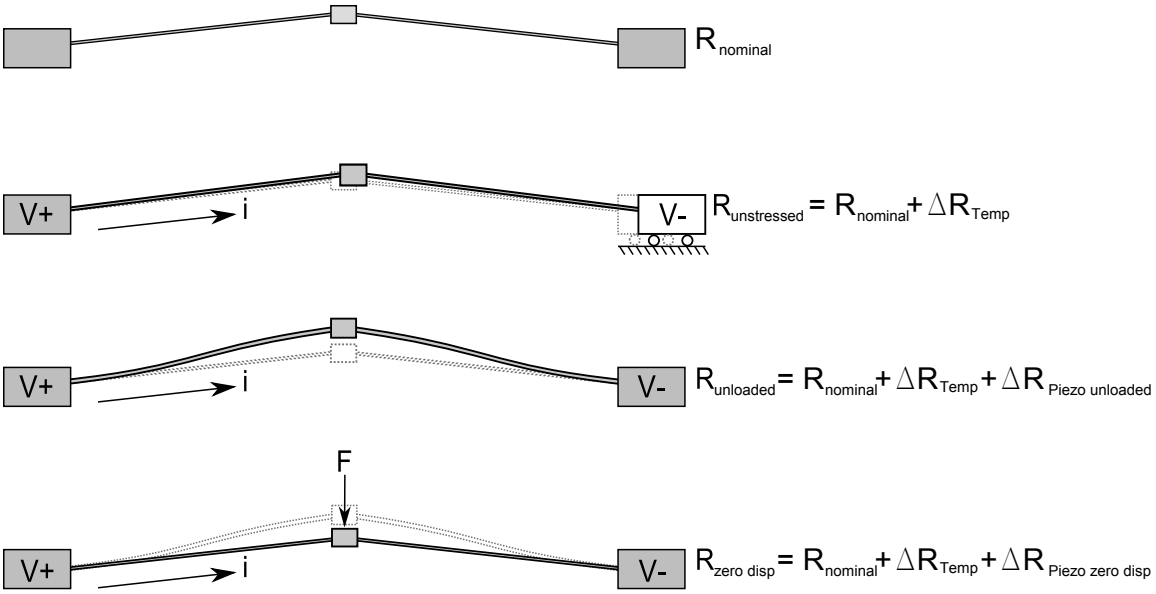

Figure 4.7: Schematic representations of four TIM states used for calibration.

calibration approach presented here finds values for α_1, α_2, π_0, and β by matching model data with experiments.

As explained in [36] the temperature dependence of a polysilicon structure can be acquired by determining the power-resistance relationship at several current levels. This relationship is used in an optimization approach that modifies the coefficients of the temperature dependence of resistivity (α_1 and α_2 of Equation 4.3) so that the model-calculated output power-resistance curve matched the measured curve from the test structure with minimum error. This approach, however, does not give a pure temperature-dependent resistivity in that other properties may be confounded. Because of this, if this approach is to be used for calibration, the calibrating structure and the device to be calibrated must be similar in heat transfer characteristics, or in-depth modeling needs to be done to account for any dissimilarities.

Therefore, it was chosen to perform the calibration measurements on the TIM itself to allow for more consistent modeling. Calibration in this way requires a complex iterative approach, as will be explained. Several variable names are first presented as background to this approach. To calibrate for the resistivity without convoluting the piezoresistive signal, an actuated, unstressed state of the TIM is necessary. However, an unstressed state

is merely hypothetical because an actuated TIM will always be stressed (see Figure 4.7). This iterative approach is in part to determine this theoretically unstressed TIM state (no piezoresistive change in resistivity). Because this is not an actual physical state that can be measured, a beginning point for the calibration will be an unloaded, but actuated, TIM, which will represent the lowest stress state for a given actuation current. The purpose of the iterative approach of calibration is to determine what offset exists between the voltages that would occur in an unstressed TIM and those measured on an unloaded TIM (see Figure 4.7).

This offset can be determined using the piezoresistive effect by determining the stress state of the unloaded TIM. However, the temperature-dependent piezoresistive coefficients need to be calibrated also. The piezoresistive coefficients are determined using data from a "fully constrained" or "zero displacement" TIM; that is, an actuated TIM that is loaded with a force so that it remains in the fabricated position (zero displacement) even with current applied (see Figure 4.7). This data will have relatively high stresses. After collecting this data at several different actuation currents, which will correspond to various temperature profiles, an optimization routine was used to determine the piezoresistive coefficients that would give the best linear fit for temperature dependence. The piezoresistive change in resistance was calculated as

$$\Delta R = R \sum \pi_i \sigma_{axial} \tag{4.6}$$

where ΔR is change in resistance, R is the original resistance, π_i is the temperature-dependent π coefficient for the i-th node, and σ_{axial} is the axial stress associated with the i-th node.

Once the piezoresistive coefficients were determined and an offset was calculated, a data set of voltages corresponding to the unstressed TIM was stored. These voltages were then used to determine the next iteration's resistivity coefficients, and the process was performed again. This process was repeated until the calculated offset converges, or in other words a converged set of theoretically unstressed TIM voltages are produced. At this point the resistivity and piezoresistivity coefficients were considered calibrated.

This iterative calibration approach incorporated a few other items to help with convergence and to reduce the effects of experimental noise. First, the routine calculated an initial guess at the theoretical unstressed voltage set using estimated piezoresistive coefficients. This was done to allow for the initial guess at the resistivity coefficients to be closer to the unstressed TIM than just merely the unloaded TIM scenario.

Second, in the calibration of the piezoresistance, the optimization goal was to minimize the error between the fractional change in resistance of the model and the test data. This was implemented by determining the fractional change in resistance of the test data and the model output between the unloaded and fully constrained cases.

Third, for the first iteration of calibration, all optimization approaches for the material properties (resistivity and piezoresistivity) used values from published sources, except the temperature dependence of piezoresistivity which was set to zero. All other iterations used the values calculated for the previous iteration as the starting values for the optimizations.

In summary, the iterative calibration technique consists of the following steps:

1. Two data sets are gathered, unloaded and fully constrained data.

2. Room temperature resistivity is calculated.

3. An initial guess at the voltages of various current inputs for a theoretically unstressed TIM is calculated by determining the piezoresistive effect that would occur for each current for an unloaded TIM. This is done using the stresses for each unloaded case, the current iteration value for the piezoresistive coefficients, and subtracting the calculated piezoresistive change from the unloaded voltage calibration data.

4. This voltage set is stored as the current guess at the voltages for the unstressed TIM.

5. The voltage set for the unstressed TIM case is then used to calculate the resistivity coefficients.

6. The resistivity coefficients and the fully constrained case calibration data are used to determine the piezoresistive coefficients for the current iteration.

Table 4.1: TIM parameters for validation testing.

Parameter	Value
Leg length	150 μm
Leg height	3.5 μm
Leg width	2.96 μm
Height above substrate	2.0 μm
Shuttle width	10 μm
Number of legs (half model)	1

7. Using the new resistivity and piezoresistivity coefficients, a new guess at the voltage set for the unstressed case is calculated.

8. Steps five through seven are iterated until the sum squared difference between the voltages of the unstressed and unloaded cases for the different current levels converges.

4.6 Validation testing

4.6.1 Testing setup

Testing was performed to show the validity of this approach for self-sensing actuation. Devices were fabricated using the MUMPs fabrication process [22]. Dimensions for the TIM tested are given in Table 4.1.

In Table 4.1 the leg width is corrected for the underetch that occurred during fabrication (0.02 μm measured using a scanning electron microscope). "Leg height" is the combined thickness of Poly1 and Poly2 layers, "height above substrate" is the thickness of the first oxide and thus the distance between the TIM legs and the substrate, and "number of legs" is the number of legs in the top grouping, or the bottom grouping, in the TIM. The test setup for the current work included a straight-line probe guide mechanism, a folded beam force gauge (0.09 μm underetch) with optical vernier, and a 1-leg TIM, see Figure 4.8. It is assumed that the difference in underetch seen here and that used for the TIM is due to the mask resolution and the fact that the beams of the force gauge were parallel to the mask orientation where as the TIM legs have a slight offset angle.

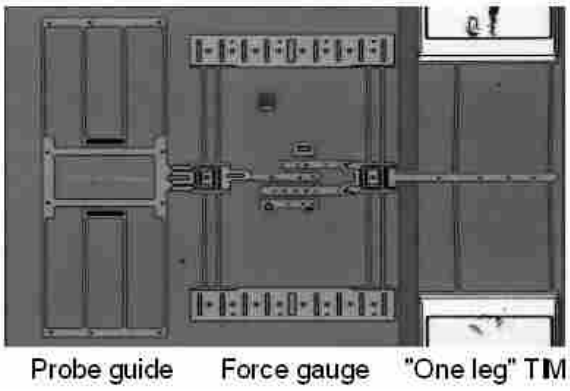

Figure 4.8: Optical microscope image of validation test setup.

Table 4.2: Unloaded case calibration data.

Current (mA)	Unloaded voltage (V) (Data set 1)	Fully constrained voltage (V) (Data set 2)
0.5000	0.3423	–
1.0000	0.6857	–
1.5000	1.0316	–
2.0000	1.3812	–
2.4999	1.7360	1.7372
3.0000	2.0913	2.0943
3.5001	2.4607	2.4665
3.9999	2.8407	2.8507
4.5001	3.2361	3.2556
5.0002	3.6613	3.6613
5.5001	4.1006	–

4.6.2 Model validation

Calibration was performed using the process described earlier on a “one leg” TIM, using voltages and currents for the unloaded and zero-displacement cases for various currents. Data sets used for calibration are given in Table 4.2. A maximum current of approximately 5.5 mA was used for this calibration. This current resulted in a maximum temperature of approximately 495 K. At higher current levels there was noticeable drift in the output measurement (see [33]). The calibration output parameter values are pre-

Table 4.3: Calibration approach output values.

Parameter	Value
ρ_0	$4.6593 \cdot 10^{-5}\ \Omega/\mathrm{m}$
α_1	$3.2787 \cdot 10^{-4}\ T^{-1}$
α_2	$1.5029 \cdot 10^{-6}\ T^{-2}$
π	$-6.3445 \cdot 10^{-5}\ \mathrm{MPa}^{-1}$
β	$2.6342 \cdot 10^{-2}\ T^{-1}$

sented in Table 4.3. These values are only useful in this study due to confounding of the piezoresistance and resistivity during the iterative calibration approach.

The full model was then run for several different current levels. Figures 4.9 and 4.10 show the model and test data for the device tested for force and displacement respectively. The dashed error bars represent the documented error for the equipment used for the electrical input and measurements during testing, or in other words error in the value of the input current to the model or error in the measured voltages that are compared to the output of the model. The solid error bars represent the error in the optical measurements made during testing of the device.

To account for drift in the instrumentation and other sources, for each current level the fully loaded voltage was determined through the model. This voltage was then corrected to be equal to the measured test voltage. This offset was then applied to all data points in the current set. This will shift the model so that the zero displacement point lines up with the test data to help account for experimental and measurement error. A further study of the drift associated with this sensing approach is needed. If drift can be reduced this correction may not be required. This correction will be done immediately before measurement to achieve the current state of drift. This could be done by using a mechanism to constrain the shuttle so that a fully constrained data point can be gathered. If this needs to be implemented then it will possibly increase the footprint of the setup and add ancillary parts and signals. However, with this correction it can be seen that for nearly all the data the model is within the measurement error.

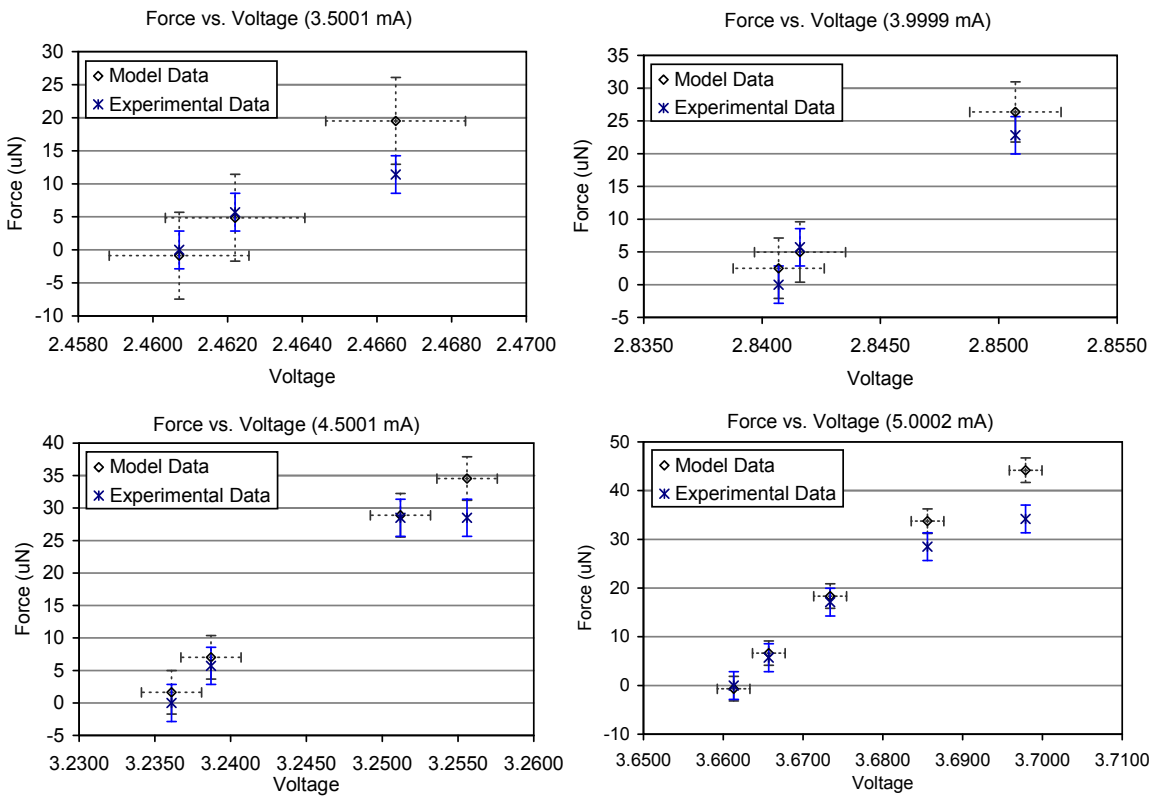

Figure 4.9: Model and testing force-voltage data comparison.

4.7 Discussion of results and future work

These results have shown high correlation between the test data and the model. There are several aspects of the data that are important to note. One complication of the mechanical analysis of this work is in the proper characterization of the boundary conditions of the legs. In the model presented here the anchor was modeled to try to represent the flexibility of the anchor during testing. However, inadequacies in this approximation could be in part responsible for discrepancies at high force and current.

Also, only four current levels are presented in this work. This is due to the fact that higher current levels experienced significant out-of-plane buckling at high force loadings, causing a zero-displacement measurement to be unobtainable (this could be changed by having constraining staples that would eliminate out-of-plane motion; however, these staples need to be placed so as to not allowing tipping of the TIM). Also, at lower current

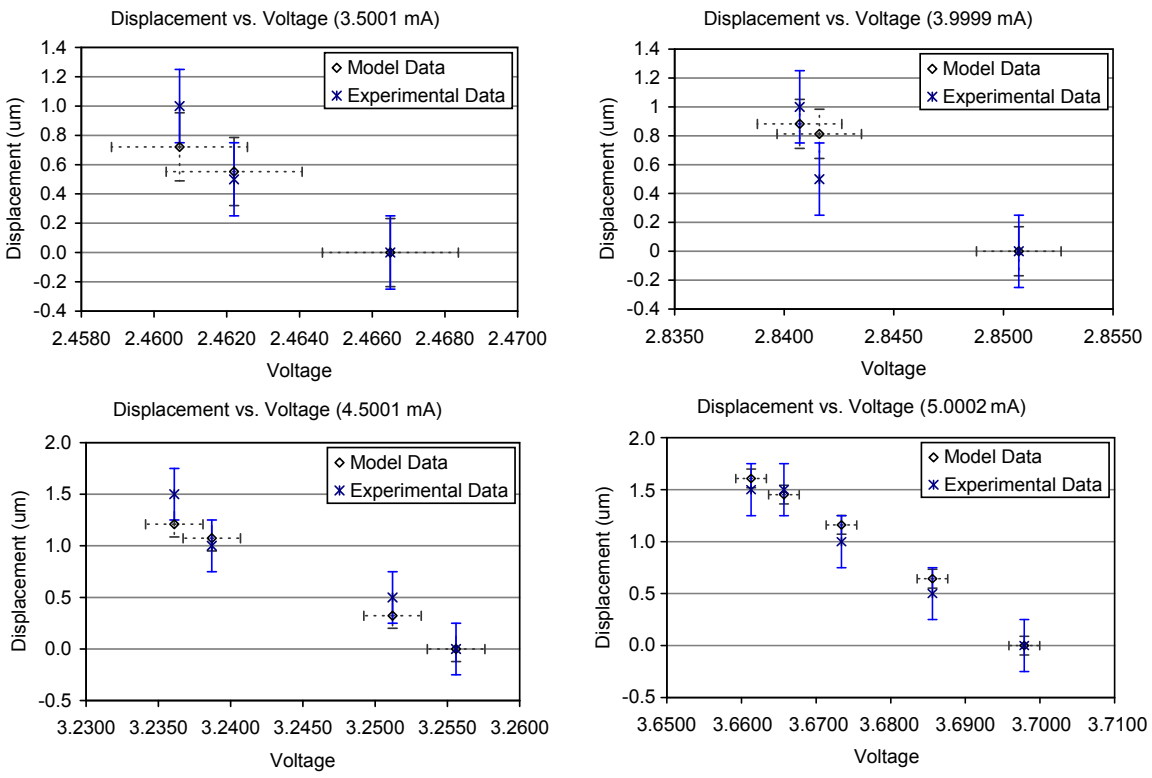

Figure 4.10: Model and testing displacement-voltage data comparison.

levels the data correlation is significant but the error in measurement becomes so large as to make the correlation inconsequential.

An initial study of drift in the TIM and measurements was done in [33]. A further study characterizing this phenomenon is needed. In this study error was reduced by taking all measurements at a particular current before proceeding to the next current. It is suggested that this be done in calibration also if possible to reduce the effects of drift in the data.

4.8 Conclusions

This paper has presented work to create a multi-physics model of the thermomechanical in-plane microactuator (TIM) for application in a self-sensing approach to actuation. This self-sensing approach used the piezoresistive property of silicon as the sensing signal. A full model has been developed and presented that couples a given stress state of

the TIM with a certain force-displacement output of a TIM. The model operates by using a measured voltage of the TIM at a given actuation current to determine the thermal and electrical states of the TIM, as well as a range of possible mechanical states. The model in this work was further developed to determine the piezoresistive changes that would occur for the range of mechanical states determined. A calibration method was presented. Validation testing performed on a "one leg" TIM design was presented with high correlation between model and test data. Ultimately, this work furthered the research toward the viability of self-sensing actuation.

4.9 Acknowledgment

This material is based upon work supported in part by the National Science Foundation under Grant No. 0428532 and DARPA through a subcontract with Block MEMS, LLC. The authors thank Michael Wilcox for his help with the piezoresistive temperature measurements.

Chapter 5

Conclusions

5.1 Thesis review

This thesis has presented work showing the viability of self-sensing for the thermomechanical in-plane microactuator (TIM). As microelectromechanical systems (MEMS) increase in popularity and complexity, improved methods of actuation and sensing are needed. Previous work showed that the the piezoresistive response of the TIM during actuation showed significant enough sensitivity to be able to allow the TIM to operate as a self-sensor. However, to realize this possibility, an adequate model of the physics of the TIM needed to be developed as well as a calibration approach. This work developed this model and calibration.

Preliminary work was done and has been presented, to expand a particular thermal modeling simplification technique for lineshape microstructures. This thermal correction (K_t) value was developed to compensate for heat losses to the surroundings including interactions between microstructures in an array (much like a multi-leg TIM). Validation testing showed good correlation between the simplified model and a full 3-dimensional model.

This K_t value was used in a finite difference model (FDM) that was developed and presented to accurately describe the thermal characteristics of the TIM. This thermal model was used to output the temperature profile of the TIM.

A finite element model (FEM) was also developed. This model used the temperature profile developed by the FDM as input to determine the mechanical state of the TIM. The FEM output included the force-displacement relationships and stress state of the TIM.

A preliminary calibration method was presented along with a novel calibration structure to account for the device-to-device variations in the temperature-dependent elec-

trical resistivity. Validation testing was presented and showed improved results over general published resistivity values.

Finally a description of the full model and new calibration approach were presented. The calibration for the final validation was done using the TIM itself as the calibrating structure. This calibration was performed in an iterative fashion using a pseudo-resistivity to calculate the current iteration's piezoresistive coefficients. The piezoresistive offset that was convoluted in the original data was then subtracted out and a new resistivity was calculated. This was repeated until the the offset converged. The output from this calibration was temperature-dependent resistivity and piezoresistivity. These calibrated material properties were then placed into the full model. The full model used a previously-developed piezoresistive modeling approach that was modified to the current work to process the expected piezoresistive response of the TIM at a given actuation current. This response was then correlated to a unique force-displacement output. Validation testing was done that showed good correlation between the model and the test data. Displacement data correlation was within the experimental error. Force data was also within the experimental error except for high voltage and currents. It is assumed that this variance may be due in part to the inadequate boundary condition assumptions. Ultimately this work has further shown the feasibility of this type of sensing, and has developed modeling and calibration approaches that will enable future work in implementation of this concept.

5.2 Future work

This work has set a significant framework for the concept of self-sensing of the TIM. As research in this area continues several items will be important:

First, it was seen through this work that certain aspects of the TIM design will be crucial to the success of this type of sensing. As has been mentioned, it is crucial that the aspect ratio of the TIM legs be such that the preferred buckling of the TIM is in the forward direction, so as to eliminate out-of-plane motion. High-aspect-ratio TIMs would be ideal. Also, if high aspect ratios are not feasible, it would be beneficial to place constraining staples over the shuttle of the TIM, while keeping the appropriate aspect ratio. These staples are to eliminate out-of-plane deflection during the loading of the TIM. It is

believed that this would help the FEM to better predict the TIM motion, and may allow a 2-dimensional beam analysis to be used instead of a 3-dimensional. If constraining staples are used without the proper aspect ratio then reaction forces caused by the staple will greatly increase the complexity of the mechanical modeling. It is suggested that two staples be used so as to eliminate the changes due to the TIM "tipping" around a single staple if out-of-plane motion does occur.

Second, several different ideas are available to acquire the temperature-dependent electrical resistivity without needing to gather unloaded data from the TIM to be used in operation. One way would be to do this calibration on a separate TIM. This was not done in the current work due to the availability of multiple TIMs on the die configuration used. Use of a separate TIM would allow either the entire calibration on a separate TIM, or it could be used merely to gather the unloaded data while performing the rest of the calibration on the TIM to be used in operation. However, there maybe complications with slight variation between TIMs. Also a novel calibration mechanism may be two competing TIMs actuating in opposite directions but with the same shuttle. Changes would need to be made to the mechanical model, but this would allow you to induce a current on one and step through currents on the other to attain different force-displacement data points for calibration. If they are actuated with the same current they would give an zero-displacement scenario.

Third, in the current work a zero-displacement loading condition was used for part of the calibration process. It is proposed that this could be done non-intrusively before operation on the TIM to be used. This could be done using a simple tethering approach. There are various ways of removing the tether, the most promising of which is to melt it using a current pulse. If this is implemented, it is important that this current does not cause higher temperatures in the main TIM than will be experienced during operation. This is because the material properties will change slightly with each successively higher temperature and would ruin the calibration. It may be that obtaining data for a zero-displacement loading will cause buckling that the FEM can not predict at the higher actuation currents. This could in part be helped by constraining the out-of-plane displacement, perhaps with staples as previously described. It may also be that an elliptic integral approach to stress

calculations for the TIM would be needed; this may be able determine the buckling that would occur.

Third, further research should be done to consider drift and repeatability of the TIM and possible ways to account for these. The drift may be compensated for by using an offset voltage measured for a given current level that is gathered before each measurement. This could be done using a mechanism to constrain the TIM, however, this would eliminate some of the benefits to this type of sensing (i.e. reduced footprint and number of electrical signals). However, if there was some other known force or displacement setting, the offset could be set by that.

Finally, it is proposed that for implementation of the TIM in a self-sensing capacity that during calibration, a reference table of voltages, currents, forces, and displacements could be developed and stored for the given TIM that would eliminate the need to run the full model every time a reading was needed. However, due to drift and changes in operating conditions an offset may need to be calculated each time to properly correlate the measured signal with the developed table.

References

[1] R. Cragun and L. Howell, "Linear thermomechanical microactuators," in *The 1999 ASME International Mechanical Engineering Congress and Exposition*, November 1999, pp. 181–188.

[2] C. Liu, *Foundations of MEMS*. Pearson Prentice Hall, 2006.

[3] R. K. Messenger, "Integrated piezoresistive sensing for feedback control of compliant MEMS," Ph.D. dissertation, Brigham Young University, 2007.

[4] T. Waterfall, K. Teichert, and B. Jensen, "Simultaneous on-chip sensing and actuation using the thermomechanical in-plane microactuator," in *DETC 2007 ASME 2007 International Design Engineering Technical Conferences*, no. DETC2007-34982, 2007.

[5] C. S. Smith, "Piezoresistance effect in germanium and silicon," *Physical Review*, vol. 94, pp. 42–49, 1954.

[6] G. K. Johns, T. L. Waterfall, L. L. Howell, B. D. Jensen, and T. W. McLain, "Exploring the resistance change trends associated with integrated piezoresistive sensing elements," in *Proceedings of SPIE - The International Society for Optical Engineering*, vol. 6529 PART 2, San Diego, CA, United States, 2007, pp. 652 938 –. [Online]. Available: http://dx.doi.org/10.1117/12.716232

[7] K. Teichert, T. Waterfall, B. Jensen, L. Howell, and T. McLain, "Piezoresistive in-line integrated force sensors for on-chip measurement and control," in *Proceedings of SPIE - The International Society for Optical Engineering*, vol. 6529 PART 2, 2007, pp. 65 292 –. [Online]. Available: http://dx.doi.org/10.1117/12.716234

[8] L. Lin and M. Chiao, "Electrothermal responses of lineshape microstructures," *Sensors and Actuators A: Physical*, vol. 55, no. 1, pp. 35–41, 1996.

[9] M. Chiao and L. Lin, "Self-buckling of micromachined beams under resistive heating," *Journal of Microelectromechanical Systems*, vol. 9, no. 1, pp. 146–151, 2000.

[10] Y. Kuang, Q. Huang, and N. Lee, "Numerical simulation of a polysilicon thermal flexure actuator," *Microsystem Technologies*, vol. 8, no. 1, pp. 17–21, 2002.

[11] A. Geisberger, N. Sarkar, M. Ellis, and G. Skidmore, "Electrothermal properties and modeling of polysilicon microthermal actuators," *Journal of Microelectromechanical Systems*, vol. 12, no. 4, pp. 513–523, 2003.

[12] Y. Lai, E. Bordatchev, S. Nikumb, and W. Hsu, "Performance Characterization of In-plane Electro-thermally Driven Linear Microactuators," *Journal of Intelligent Material Systems and Structures*, vol. 17, no. 10, p. 919, 2006.

[13] L. Que, J.-S. Park, and Y. Gianchandani, "Bent-beam electrothermal actuators-part I: Single beam and cascaded devices," *Journal of Microelectromechanical Systems*, vol. 10, no. 2, pp. 247 – 254, 2001.

[14] C. D. Lott, T. W. McLain, J. Harb, and L. L. Howell, "Modeling the thermal behavior of a surface-micromachined linear-displacement thermomechanical microactuator," *Sensors and Actuators, A: Physical*, vol. 101, no. 1–2, pp. 239 – 250, 2002.

[15] J. Maloney, D. Schreiber, and D. DeVoe, "Large-force electrothermal linear micromotors," *Journal of Micromechanics and Microengineering*, vol. 14, no. 2, pp. 226–234, 2004.

[16] E. Enikov, S. Kedar, and K. Lazarov, "Analytical Model for Analysis and Design of V-Shaped Thermal Microactuators," *Journal of Microelectromechanical Systems*, vol. 14, no. 4, pp. 788–798, 2005.

[17] M. Sinclair, "A high force low area MEMS thermal actuator," *The Seventh Intersociety Conference on Thermal and Thermomechanical Phenomena in Electronic Systems. ITHERM 2000.*, vol. 1, pp. 127–132, 2000.

[18] R. K. Messenger, "Modeling and control of surface micromachined thermal actuators," Master's thesis, Brigham Young University, Provo, UT, 2004.

[19] Q.-A. Huang and N. K. S. Lee, "Analysis and design of polysilicon thermal flexure actuator," *Journal of Micromechanics and Microengineering*, vol. 9, no. 1, pp. 64 – 70, 1999.

[20] D. Yan, A. Khajepour, and R. Mansour, "Modeling of two-hot-arm horizontal thermal actuator," *Journal of Micromechanics and Microengineering*, vol. 13, no. 2, pp. 312–322, 2003.

[21] J. N. Harb, S. M. Lyon, J. Larsen, L. L. Howell, and T. W. McLain, "Design factors influencing power reduction in thermomechanical in-plane microactuators (DETC2007-34206)," in *DETC 2007 ASME 2007 International Design Engineering Technical Conferences*, 2007.

[22] D. A. Koester, R. Mahadevan, B. Hardy, and K. Markus, *MUMPs Design Handbook, Rev. 5.0*. Cronos Integrated Microsystems, 2000. [Online]. Available: http://www.memsrus.com.

[23] Sandia National Laboratories, "Summit V™." [Online]. Available: http://mems.sandia.gov/tech-info/summit-v.html

[24] K. Teichert and B. Jensen, "Thermal correction values for analysis of lineshape microstructure arrays," *Submitted for review: Sensors and actuators. A, Physical*, 2008.

[25] D. Bell, T. Lu, N. Fleck, and S. Spearing, "MEMS actuators and sensors: observations on their performance and selection for purpose," *Journal of Micromechanics and Microengineering*, vol. 15, no. 3, 2005.

[26] J.-S. Park, L. Chu, E. Siwapornsathain, A. Oliver, and Y. Gianchandani, "Long throw and rotary output electro-thermal actuators based on bent-beam suspensions," *Proceedings of the IEEE Micro Electro Mechanical Systems (MEMS)*, pp. 680 – 685, 2000.

[27] R. Johnstone and M. Parameswaran, "Modelling surface-micromachined electrothermal actuators," *Electrical and Computer Engineering, Canadian Journal of*, vol. 29, no. 3, pp. 193–202, 2004.

[28] S. Chen and M. Culpepper, "Design of Contoured Micro-scale Thermomechanical Actuators," *Microelectromechanical Systems, Journal of*, vol. 15, no. 5, pp. 1226–1234, 2006.

[29] C. Lott, T. McLain, J. Harb, and L. Howell, "Modeling the thermal behavior of a surface-micromachined linear-displacement thermomechanical microactuator," *Sensors & Actuators: A. Physical*, vol. 101, no. 1-2, pp. 239–250, 2002.

[30] M. Buehler, S. Grant, and W. Thurber, "Bridge and van der Pauw Sheet Resistors for Characterizing the Line Width of Conducting Layers," *Journal of The Electrochemical Society*, vol. 125, p. 650, 1978.

[31] Y. Okada and Y. Tokumaru, "Precise determination of lattice parameter and thermal expansion coefficient of silicon between 300 and 1500 K," *Journal of Applied Physics*, vol. 56, p. 314, 1984.

[32] N. B. Hubbard and L. L. Howell, "Experimental repeatability of a thermal actuator for nanopositioning," Anaheim, CA, United States, 2004, pp. 427 – 430.

[33] T. Waterfall, "Design of piezoresistive mems force and displacement sensors," Master's thesis, Brigham Young University, 2006.

[34] J. W. Wittwer, "Simulation-based design under uncertainty for compliant microelectromechanical systems," Ph.D. dissertation, Brigham Young University, Provo, UT, 2005.

[35] J. W. Wittwer, T. Gomm, and L. L. Howell, "Surface micromachined force gauges: uncertainty and reliability," *Journal of Micromechanics and Microengineering*, vol. 12, pp. 13–20, 2002.

[36] K. Teichert and B. Jensen, "Calibration approach for thermomechanical in-plane microactuator self-sensing," in *Accepted and pending publication: DETC 2008 ASME 2008 International Design Engineering Technical Conferences*, no. DETC2007-49546, 2008.

[37] J. Grade, H. Jerman, and T. Kenny, "Design of large deflection electrostatic actuators," *Microelectromechanical Systems, Journal of*, vol. 12, no. 3, pp. 335–343, 2003.

[38] F. P. Incropera and D. P. DeWitt, *Fundamentals of Heat and Mass Transfer*, 5th ed. John Wiley and Sons, 2002.

[39] T. Waterfall, K. Teichert, and B. Jensen, "Simultaneous on-chip sensing and actuation using the thermomechanical in-plane microactuator," *Submitted for review: The Journal of Microelectromechanical Systems (JMEMS)*, 2008.

[40] T. Waterfall, G. Johns, R. Messenger, B. Jensen, T. McLain, and L. Howell, "Observations of piezoresistivity for polysilicon in bending that are unexplained by linear models," *Sensors & Actuators: A. Physical*, vol. 141, no. 2, pp. 610–618, 2008.

[41] G. Johns, L. Howell, B. Jensen, and T. McLain, "A Model for Predicting the Piezoresistive Effect in Microflexures Experiencing Bending and Tension Loads," *Microelectromechanical Systems, Journal of*, vol. 17, no. 1, pp. 226–235, 2008.

[42] J. Y. Seto, "Piezoresistive properties of polycrystalline silicon," *Journal of Applied Physics*, vol. 47, no. 11, pp. 4780–4783, 1976.

[43] F. J. Morin, T. Geballe, and C. Herring, "Temperature dependence of the piezoresistance of high-purity silicon and germanium," *Physical Review*, vol. 105, pp. 525–539, 1957.

[44] V. Gridchin, V. Lubimsky, and M. Sarina, "Piezoresistive properties of polysilicon films," *Sensors and Actuators A: Physical*, vol. 49, no. 1, pp. 67–72, 1995.

[45] C. Cho, R. Jaeger, and J. Suhling, "Experimental characterization of the temperature dependence of the piezoresistive coefficients of silicon," *Thermal and Thermomechanical Phenomena in Electronics Systems, 2006. ITHERM'06. The Tenth Intersociety Conference on*, pp. 928–935, 2006.

[46] O. Tufte and E. Stelzer, "Piezoresistive properties of silicon diffused layers," *Journal of Applied Physics*, vol. 34, pp. 313–318, 1963.